Cell

Article

Inhibition of oligomeric BAX by an anti-apoptotic dimer

Graphical abstract

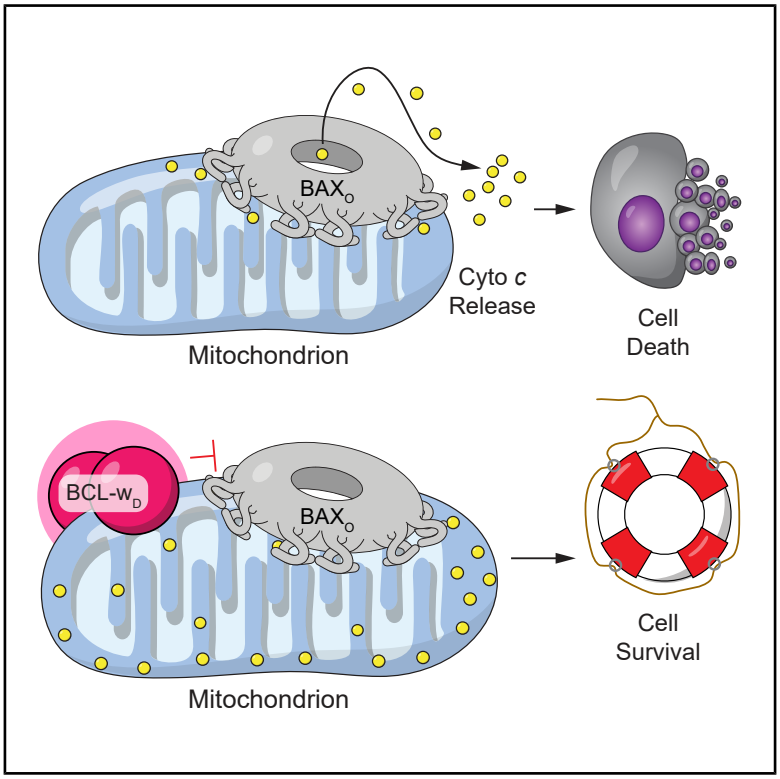

Authors

Catherine E. Newman, Micah A. Gygi, Haleh Alimohamadi, ..., Gerard C.L. Wong, Thomas E. Wales, Loren D. Walensky

Correspondence

loren_walensky@dfci.harvard.edu

In brief

A full-length dimeric form of the anti-apoptotic protein BCL-w can block oligomeric BAX-driven mitochondrial permeabilization and apoptosis, revealing a new layer of cell-death control.

Highlights

- BAX oligomers (BAX$_O$) can be directly dissociated by dimeric BCL-w (BCL-w$_D$)
- Dimeric but not monomeric BCL-w can block BAX$_O$-mediated mitochondrial apoptosis
- BCL-w$_D$ neutralizes the membrane-disruptive negative curvature induced by BAX$_O$
- Beyond the heterodimer paradigm, apoptosis is regulated by multimeric interactions

Newman et al., 2025, Cell *188*, 1–16
December 24, 2025
https://doi.org/10.1016/j.cell.2025.10.037

CellPress

Cell

CellPress

Article

Inhibition of oligomeric BAX by an anti-apoptotic dimer

Catherine E. Newman,[1,7] Micah A. Gygi,[1,7] Haleh Alimohamadi,[2] Thomas M. DeAngelo,[1] Christina M. Camara,[1] Julian Mintseris,[3] Ezra Yu,[1] Edward P. Harvey,[1] Zachary J. Hauseman,[1] Lixin Fan,[4] Yun-Xing Wang,[5] Elizabeth W.-C. Luo,[2] Marina Godes,[1] Jacob Gehtman,[1] Ann M. Cathcart,[1] Steven P. Gygi,[3] John R. Engen,[6] Gregory H. Bird,[1] Gerard C.L. Wong,[2] Thomas E. Wales,[6] and Loren D. Walensky[1,8,*]

[1]Department of Pediatric Oncology and Chemical Biology Program, Dana-Farber Cancer Institute, Boston, MA 02215, USA
[2]Department of Bioengineering, University of California, Los Angeles, Los Angeles, CA 90095, USA
[3]Department of Cell Biology, Harvard Medical School, Boston, MA 02115, USA
[4]SAXS Facility, Center for Cancer Research, National Cancer Institute, Frederick, MD 21702, USA
[5]Center for Structural Biology, Center for Cancer Research, National Cancer Institute, Frederick, MD 21702, USA
[6]Department of Chemistry and Chemical Biology, Northeastern University, Boston, MA 02115, USA
[7]These authors contributed equally
[8]Lead contact
*Correspondence: loren_walensky@dfci.harvard.edu
https://doi.org/10.1016/j.cell.2025.10.037

SUMMARY

BAX is a pro-apoptotic BCL-2 protein that resides in the cytosol as a monomer until triggered by cellular stress to form an oligomer that permeabilizes mitochondria and induces apoptosis. The paradigm for apoptotic blockade involves heterodimeric interactions between pro- and anti-apoptotic monomers. Here, we find that full-length BCL-w forms a distinctive, symmetric dimer (BCL-w_D) that dissociates oligomeric BAX (BAX_O), inhibits mitochondrial translocation, promotes retrotranslocation, blocks membrane-porating activity, and influences apoptosis induction of cells. Structure-function analyses revealed discrete conformational changes upon BCL-w dimerization and reciprocal structural impacts upon BCL-w_D and BAX_O interaction. Small-angle X-ray scattering (SAXS) analysis demonstrated that BAX_O disrupts membranes by inducing negative Gaussian curvature, which is reversed by positive Gaussian curvature exerted by BCL-w_D. Systematic truncation and mutagenesis dissected the core features of BCL-w_D activity—dimerization, BAX_O engagement, and membrane interaction. Our studies reveal a downstream layer of apoptotic control mediated by protein and membrane interactions of higher-order BCL-2 family multimers.

INTRODUCTION

Apoptosis is a form of programmed cell death that determines cell fate in response to stress, and its deregulation underlies myriad diseases from cancer to neurodegeneration.[1] B cell lymphoma 2 (BCL-2) family proteins orchestrate this decision by regulating the integrity of the mitochondrial outer membrane (MOM). The essential ''executioner'' proteins are pro-apoptotic BCL-2-associated X (BAX) and BCL-2 antagonist/killer 1 (BAK), which, upon activation, undergo a conformational transformation from monomers to oligomers that permeabilize the MOM.[2] Loss of mitochondrial integrity releases cytochrome *c* and other factors into the cytosol,[3] committing the cell to apoptotic death. A critical step in BAX/BAK activation is exposure of their BCL-2 homology 3 (BH3) α-helices, which either drive self-association and death or are intercepted by anti-apoptotic BCL-2 proteins, resulting in heterodimeric blockade.[4,5] An FDA-approved inhibitor of this canonical interaction reactivates apoptosis in cancer,[6,7] highlighting the importance of dissecting BCL-2 protein interactions to guide next-generation therapeutics.

Beyond BH3-in-groove inhibition, additional mechanisms regulate BAX activation. The BH4 motif of select anti-apoptotic members can stabilize monomeric BAX by binding a discrete site[8] that lies adjacent to another location targeted by the cytomegalovirus viral mitochondria-localized inhibitor of apoptosis (vMIA) protein, which suppresses BAX activation to promote host-cell survival during infection.[9] Another inhibitory pathway, BCL-X_L-mediated retrotranslocation, shuttles BAX from mitochondria to cytosol by an undefined mechanism.[10,11] A lingering mystery is how homologous proteins of such similar structure enact opposing functions,[12] with progress limited by the lack of high-resolution structures of full-length, higher-order multimers, which hold the key to unlocking fundamental insights.

Recent structural and biochemical advances have begun to close this gap. A high-resolution structure of oligomeric BAX revealed asymmetric α2-α9 dimers that tetramerize into repeating units.[13] Previously, we produced and characterized a

Please cite this article in press as: Newman et al., Inhibition of oligomeric BAX by an anti-apoptotic dimer, Cell (2025), https://doi.org/10.1016/j.cell.2025.10.037

homogeneous, full-length oligomeric BAX species (BAX_O) by treating monomeric BAX (BAX_M) with Fos-12, yielding a ~150-kDa oligomer that persisted after detergent removal and delineated structural determinants of discrete steps along the BAX-activation pathway.[14] We applied the same workflow to anti-apoptotic BCL-w and observed dimer rather than oligomer formation and no membrane-disruptive effect.[14] Monomeric BCL-w inhibited MOM by BH3-triggered BAX_M but not by BAX_O, indicating that BAX_O conformation was beyond its inhibitory control. Although dimers of anti-apoptotic truncates have been observed under various experimental conditions,[15,16] their physiologic relevance remains unknown. Here, we interrogated whether a full-length anti-apoptotic dimer can regulate apoptosis through a non-canonical mechanism, specifically by modulating the oligomerization state and function of BAX.

RESULTS

Detergent-induced self-association of full-length BCL-w is distinct from BAX

To examine the behavior of anti-apoptotic BCL-w under the conditions that induce BAX_O formation, we incubated full-length BAX_M (aa 1–192) and full-length monomeric BCL-w ($BCL\text{-}w_M$) (aa 1–193) with Fos-12—a detergent used to generate BAX_O—and examined their size exclusion chromatography (SEC) elution profiles. Whereas Fos-12 transformed BAX from a ~20 kDa monomer (BAX_M) to a ~150 kDa oligomer (BAX_O) (Figures 1A and 1B), treatment of $BCL\text{-}w_M$ with Fos-12, in addition to other detergents, produced a stable dimeric species ($BCL\text{-}w_D$) of 42 kDa, as confirmed by SEC-multi-angle light scattering (MALS) (Figures 1C, 1D, and S1A–S1C).

To systematically dissect the determinants of BCL-w dimerization, we started with an α2-α5 truncate that forms a core dimeric component of higher-order BAX oligomers (Figure 1E).[13,17,18] In contrast to GFP-BAX α2-α5 (aa 53–128 C62S/C126S),[18] GFP-BCL-w α2-α5 (aa 42–112 C107S) remained monomeric without detergent (Figure 1F), suggesting an alternate mechanism of dimerization. To identify the portion of BCL-w required for detergent-induced dimerization, we sequentially expanded the truncate from α1-α5 to α1-α6 and α1-α8 and observed that only α1-α8 dimerized upon addition of Fos-14 (Figure 1G), a detergent that produced the most monodispersed and homogeneous peak of full-length $BCL\text{-}w_D$ by SEC (Figures S1A and S1B). To verify this finding without the GFP-tagged system, we tested the dimerization potential of BCL-wΔC (aa 1–156; α1-α8), BCL-wΔN (aa 40–193; α2-α9), and BCL-wΔNΔC (aa 40–156; α2-α8). All three constructs dimerized, thus defining α2-α8 as the minimal region required (Figure 1H). These data point to a mechanism of BCL-w dimeric self-assembly distinct from BAX and BAK, with an unexpected role of α7-α8.

To confirm the presence of BCL-w dimers in cells, we generated lysates from p185+ $Arf^{-/-}$ murine B cell acute lymphoblastic leukemia (B-ALL) cells engineered to require full-length, FLAG-tagged BCL-w expression for cell survival[19] and observed that BCL-w predominantly migrated as a dimer (Figures S1B and S1D). To confirm homo-dimerization in cells, we co-expressed V5- and FLAG-tagged constructs of full-length BCL-w in HEK 293T cells (Figure S1E) and performed reciprocal co-immunoprecipitation experiments. In each case, anti-V5 and anti-FLAG immunoprecipitations pulled down both tagged species, indicative of BCL-w homo-dimerization (Figure S1F). These data are consistent with prior observations of anti-apoptotic BCL-2 protein dimers (of unknown function) in cells.[20,21]

Characterization of the structural transformation from monomeric to dimeric BCL-w

To assess the solution structure of $BCL\text{-}w_D$, we used in-line SEC combined with small-angle X-ray scattering (SAXS) (Figure 1I). The linearity of the Guinier plot indicates monodispersity without aggregation in solution (Figure 1J). The estimated molecular weights of $BCL\text{-}w_D$ (42.5 or 47.6 kDa, depending on the calculation method) confirmed that $BCL\text{-}w_D$ is a dimer in solution (Figure 1K). The asymmetrical $P(r)$ distribution, with two peaks shifted to the lower r region, indicates that $BCL\text{-}w_D$ has a multi-domain and elongated shape (Figure 1L), consistent with its SEC elution at a higher apparent molecular weight on Superdex 200 (S200) compared with Superose 6 (S6) (Figures S1A and S1B). The SAXS-derived molecular envelope revealed an elongated, symmetric dimer (Figure 1M), reflecting a conformational rearrangement from $BCL\text{-}w_M$ (Figure 1C). In contrast to the X-ray structure of a C-terminally truncated $BCL\text{-}X_L$ dimer,[16] which demonstrates an elongated α5-α6 helix with linear overlap at the center of the dimer flanked by globular ends (Figure S1G), here we observe the opposite for full-length $BCL\text{-}w_D$, with the globular portion juxtaposed at the center of the dimer and more linear portions extending outward in opposite directions (Figure 1M).

To model a conformational arrangement for $BCL\text{-}w_D$ compatible with the SAXS-derived molecular envelope, we performed molecular dynamics (MD) simulations. As a starting point, we used the crystal structure of a truncated and point-mutated BCL-w dimer, which features a distinctive domain-swapped architecture whereby helices α3 and α4 from each monomer hinge outward and cross into the partner protomer to engage the contralateral α5-α6 hairpin (Figure S1H).[15] This rearrangement is enabled by flexible hinge regions between α2-α3 and α4-α5, which reorient the helical segments into a more extended conformation (Figure S1H). Prior to simulation, we rebuilt the missing N- and C-terminal residues and reverted the point mutations to generate a wild-type (WT), full-length species. The system was fully relaxed, allowing the model to explore conformational space and adapt to the SAXS-derived envelope, capturing potential dynamic features and deviations from the crystal conformation otherwise present in solution. What emerged was a domain-swapped architecture observed crystallographically but with modified helical pitches and interprotomer spacings, reflecting a significant structural deviation from the compact monomeric fold (Figures 1N and 1O). The globular core is composed of the α5-α6 hairpin of one protomer engaging the α3-α4 hairpin of the opposite protomer, each α5-α6 hairpin aligned nearly perpendicular to its α3-α4 partner. Intriguingly, both α5-α6 hinges are oriented in the same direction, ideally positioned for symmetric membrane engagement. These core helices are bookended on each side of the dimer by the confluence of α1, α2, α7, and α8. The components of the SAXS-derived envelope that project outward from the globular core are

Please cite this article in press as: Newman et al., Inhibition of oligomeric BAX by an anti-apoptotic dimer, Cell (2025), https://doi.org/10.1016/j.cell.2025.10.037

CellPress

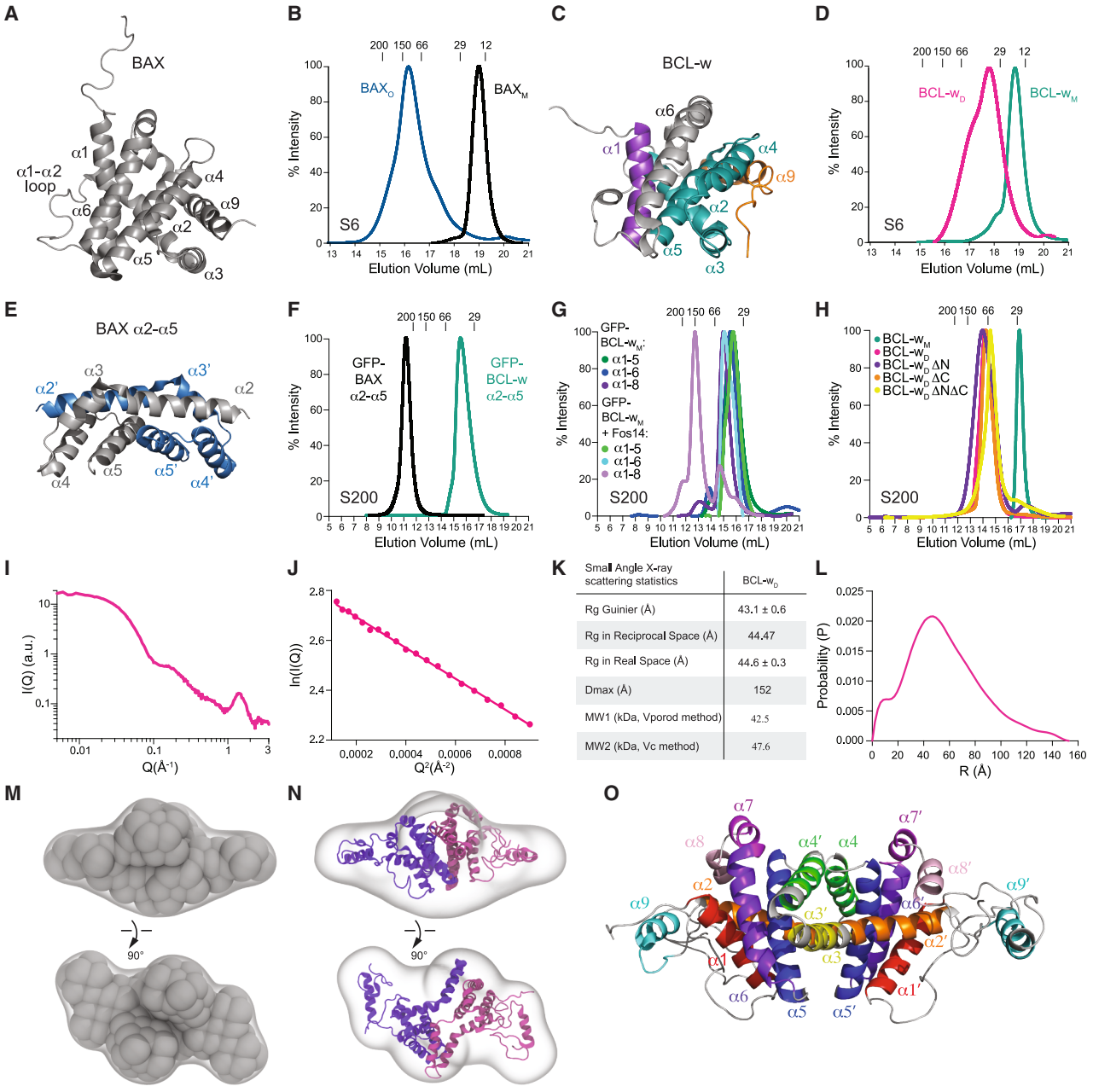

Figure 1. Production and characterization of a full-length BCL-w dimer

(A) Structure of BAX$_M$ (aa 1–192, PDB: 1F16).

(B) Fos-12 treatment of BAX$_M$ (black) yields BAX$_O$ (blue) of ~150 kDa by SEC.

(C) Structure of BCL-w$_M$ lacking 10 C-terminal residues (aa 1–183, PDB: 1O0L), demonstrating a similar overall fold as BAX.

(D) Fos-12 treatment of BCL-w$_M$ (aa 1–193) (teal) yields BCL-w$_D$ (pink) of ~40 kDa by SEC.

(E) Structure of dimeric BAX α2-α5 (aa 53–128 C62S/C126S, PDB: 4BDU).

(F) Expression and purification of GFP-BAX α2-α5 (aa 53–128, black, 37 kDa) yielded a dimer of BAX dimers (tetramerization mediated by GFP), but the analogous preparation of GFP-BCL-w α2-α5 (aa 42–112, teal, 36 kDa) produced a monomer.

(G) GFP-BCL-w α1-α5 and α1-α6 remain monomeric in the presence (light green and light blue) or absence (dark green and dark blue) of Fos-14. GFP-BCL-w α1-α8 (dark purple) dimerizes in response to Fos-14 treatment (light purple).

(H) N-terminal (aa 1–39), C-terminal (aa 157–193), or dual N-/C-truncation of BCL-w does not prevent dimerization, as evidenced by the similar SEC elution profiles of Fos-14-treated BCL-w$_D$ΔN (purple), BCL-w$_D$ΔC (orange), BCL-w$_D$ΔNΔC (yellow), and BCL-w$_D$ (pink).

(I–M) SAXS analysis of BCL-w$_D$ (I), including Guinier plot (J), size and spatial characteristics (K), plot of *P*(r) versus particle radius (*r*) (L), and 3D envelope (M).

(N and O) MD-derived model of full-length BCL-w$_D$ within the 8 Å shell (N) and its structural features (O).

See also Figures S1 and S2 and Video S1.

Please cite this article in press as: Newman et al., Inhibition of oligomeric BAX by an anti-apoptotic dimer, Cell (2025), https://doi.org/10.1016/j.cell.2025.10.037

occupied by portions of the unstructured N terminus and α1-α2 loop and the C-terminal region of each protomer (Figures 1N and 1O). This MD-derived structure is consistent with α2-α8 representing a key self-association component of the dimer (Figures 1F–1H), with the N- and C-terminal regions projecting outward and thus accessible for interaction.

To probe the relative conformational stability and consistency of the calculated model structure, we compared simulations within 8, 10, and 12 Å shells. In each case, the dimeric species rapidly equilibrated and converged on an overall similar fold, as reflected both by highly consistent difference distance matrix plots (DDMPs) when compared with the crystal structure of a truncated BCL-w dimer[15] and per-residue root-mean-square fluctuations (RMSFs) of α-carbons (Figures S2A–S2G). Upon removing the constraints of the SAXS shell, two predominant conformers emerged: an extended version mirroring that observed within the SAXS shell and a more compact species that results from the C-terminal region bearing down on the nearby surface composed of α1 and α2 and the adjacent α3-α4 hairpin (Figures S2H and S2I; Video S1). Mapping the surface electrostatic potential revealed that the compact form consolidates the distinctive charge distribution of BCL-w_D, forming an electrostatic funnel that could drive dimeric assembly and stability (Figure S2J).

To corroborate these SAXS/MD findings and investigate the conformational changes induced by dimerization, we performed hydrogen deuterium exchange mass spectrometry (HDX-MS). Prominent and persistent regions of conformational deprotection upon dimer formation occurred at the N terminus of BCL-w, including α1, the α1-α2 loop, and α2 (Figures 2A–2C; Data S1). Notably, α1 and the α1-α2 loop were previously observed to be key regions of deprotection upon conversion of BAX_M to BAX_O.[14] Additional changes upon BCL-w dimerization included deprotection of the α2-α3 and α4-α5 hinges (the very regions that must pivot to permit α3-α4 hairpin exchange), the α5-α6 hairpin, and the α7-α8 hinge, and transient protection of proximal α3, the α8-α9 loop, and α9 (Figures 2A–2C). The HDX-MS data validate that BCL-w undergoes a major conformational change upon dimerization, with striking alterations across the N-terminal region, junctions of the domain-swapped α3-α4 hairpin, α5-α6 hairpin, and C terminus.

To further investigate this structural transformation, we performed chemical crosslinking and MS analyses, comparing the proximity of BCL-w residues before and after dimerization. We subjected BCL-w_M and BCL-w_D to chemical reagents that either crosslink amine (K) or acidic (D and E) residues within a distance range of 7.7–20.4 Å[14,22] (Table S1A). After SDS-PAGE separation of crosslinked BCL-w_M and BCL-w_D, MS analyses were performed on the monomeric bands to detect intramolecular crosslinks enriched in the monomeric versus dimeric states. To validate our method, we mapped the BCL-w_M-enriched crosslinks onto the BCL-w NMR structure (PDB: 1O0L) and, after accounting for conformational flexibility of loop regions, we confirmed that the identified crosslinks were compatible with the NMR structure of BCL-w_M (Figure 2D; Table S1B; Data S2). Upon formation of BCL-w_D, there was a prominent decrease in discrete crosslinks between α2 and α9 and enrichment of crosslinks (1) within α1 and between α1 and the α1-α2 loop and between (2) α1 and α2, (3) the α1-α2 loop and α2, (4) α2 and α3, and (5) α1 and α9 (Figure 2E; Table S1C; Data S2). Comparative mapping of these newfound crosslinks onto the NMR structure of BCL-w_M and the MD-derived structure of BCL-w_D revealed predominant compatibility with the dimeric species (Table S1C; Data S2). These crosslinking data are consistent with prominent exposure of the α1/α2 region upon dimerization, as detected by HDX-MS (Figures 2A–2C), and further indicate that this conformational change brings the N-terminal region in closer proximity to itself and to α3, α4, and α9 within the monomeric units of BCL-w_D.

Dimeric BCL-w inhibits BAX_O

Given the yin-and-yang relationship between pro- and anti-apoptotic monomers, we hypothesized that higher-order forms may interact to provide a further layer of regulation within the MOM. To test this hypothesis, we generated fluorescent BAX_O trackable by fluorescence SEC (FSEC). Whereas incubating fluorescein isothiocyanate (FITC)-BAX_O with BCL-w_M had little to no effect on its elution profile, exposure to BCL-w_D completely converted FITC-BAX_O to a lower-order species (Figure 3A). These data suggest that direct interaction between BCL-w_D and BAX_O disrupted the higher-order oligomerization state of BAX. To validate this result by a distinct experimental method, we performed chemical crosslinking with 1-ethyl-3-(3-dimethylaminopropyl)carbodiimide hydrochloride (EDC) of BAX_O alone and in the presence of BCL-w_M or BCL-w_D, and then monitored BAX migration by reducing gel electrophoresis and silver stain. Again, we observed little to no change in the BAX_O oligomerization state upon incubation with BCL-w_M but near complete elimination of higher-order BAX species upon crosslinking in the presence of BCL-w_D (Figure 3B). The identical result was obtained with added liposomes mimicking the MOM[23] (Figures S3A and S3B). Western analyses confirmed that BAX_O was indeed converted to lower molecular weight species that contained BCL-w upon incubation with BCL-w_D but not BCL-w_M (Figures 3C and 3D). Of note, detected species reflect conformers accessible to the crosslinker, whereas other assemblies may not be trapped under these conditions.

We next assessed whether BCL-w_D inhibition of BAX oligomerization suppressed BAX-mediated mitochondrial apoptosis by monitoring cytochrome *c* release from liver mitochondria of $AlbCre^{pos}Bax^{f/f}Bak^{-/-}$ mice.[24] Whereas BCL-w_M had no inhibitory effect on BAX_O-mediated cytochrome *c* release, BCL-w_D caused dose-responsive inhibition (Figure 3E). To determine if the BCL-w_D mechanism involved the canonical groove, we introduced a G94E mutation, previously shown to abrogate monomeric function,[25] and confirmed that it eliminated BCL-w's ability to block truncated BH3 interacting domain death agonist (tBID)-triggered, BAX_M-mediated cytochrome *c* release (Figure 3F). However, G94E mutagenesis did not prevent Fos-14-induced dimerization of BCL-w (Figure S3C), nor did it disrupt the capacity of BCL-w_D G94E to dose-responsively block BAX_O-mediated cytochrome *c* release (Figure 3G). As an orthogonal approach, we further tested the effect of ABT-737, a small molecule that inhibits BCL-w,[6] on the function of monomeric and dimeric BCL-wΔC, using the C-terminally deleted form to maximize ABT-737 targeting of the canonical groove. Consistent with

Please cite this article in press as: Newman et al., Inhibition of oligomeric BAX by an anti-apoptotic dimer, Cell (2025), https://doi.org/10.1016/j.cell.2025.10.037

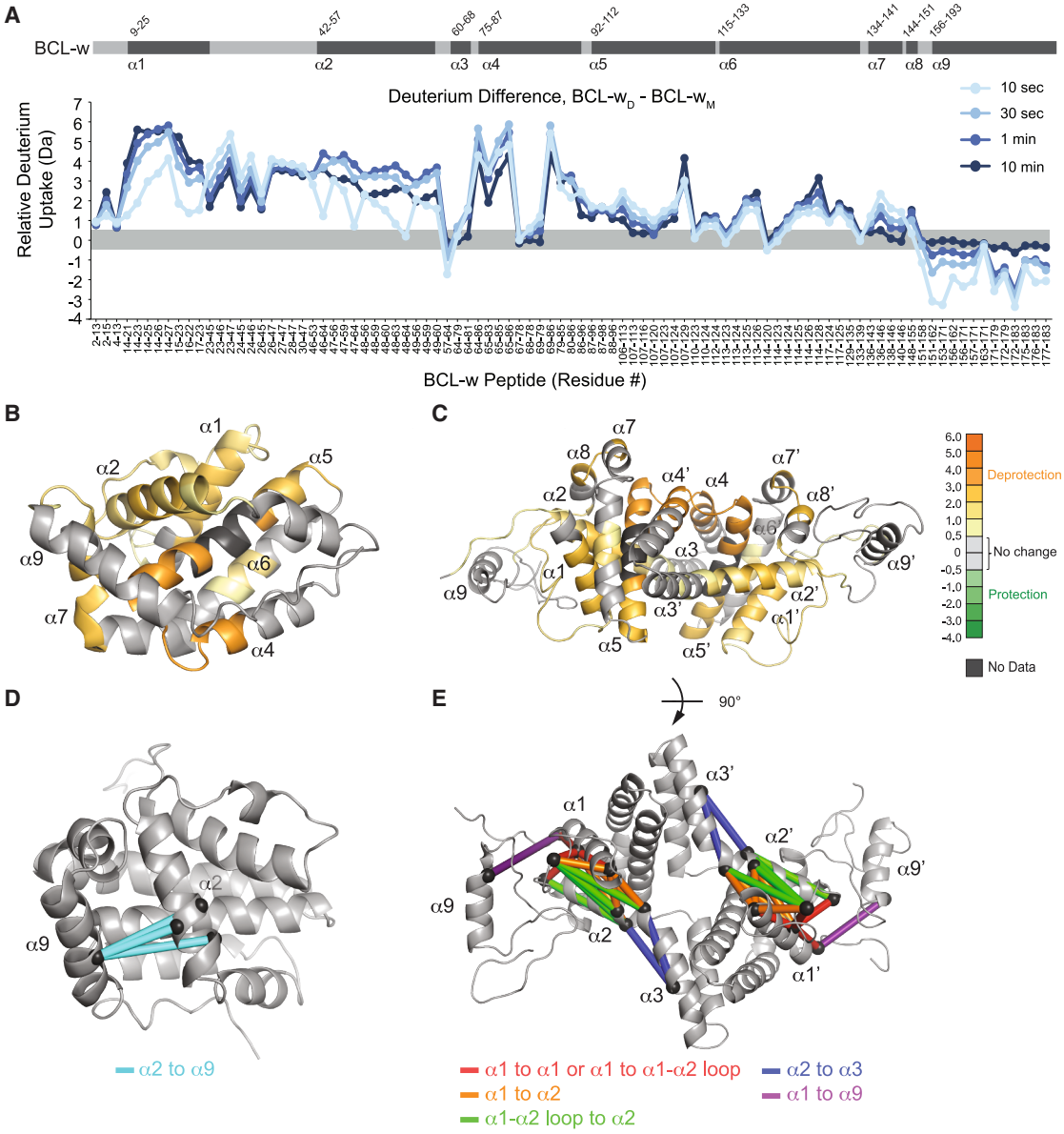

Figure 2. Analysis of the conformational transformation of monomeric to dimeric BCL-w by HDX-MS

(A–C) Deuterium difference plot showing the relative deuterium incorporation of BCL-w$_D$ minus BCL-w$_M$ as measured over time in solution (A), with areas of conformational deprotection (increased exchange, orange scale) and protection (decreased exchange, green scale) at 10 min (significance threshold, ±0.5 Da) mapped onto BCL-w$_M$ (PDB: 1O0L) (B) and MD-derived BCL-w$_D$ (C). Data are representative of at least four biological replicates.

(D and E) To compare the proximity of structural regions in the monomeric unit of BCL-w before and after dimerization, MS analyses were performed on chemically crosslinked BCL-w$_M$ and BCL-w$_D$, and crosslinks 10-fold or more enriched in the monomeric versus dimeric states were identified. Crosslinks satisfying linker-length constraints are mapped onto BCL-w$_M$ (PDB:D 1O0L) (D) and MD-derived dimer (E).

See also Data S1 and S2 and Table S1.

the G94E experiments, ABT-737 dose-responsively blocked BCL-w$_M$ inhibition of tBID-triggered, BAX$_M$-mediated cytochrome *c* release but had no disruptive effect on dimerization (Figure S3D) or BCL-w$_D$ inhibition of BAX-mediated cytochrome *c* release (Figure 3H). These data indicate that BCL-w$_D$ directly interacts with BAX$_O$, disrupts its higher-order oligomerization, and inhibits its mitochondrial membrane-permeabilizing function. Importantly, the activity of BCL-w$_D$ is independent of the canonical groove, such that neither G94E mutagenesis nor ABT-737 disrupts dimerization or its capacity to inhibit BAX$_O$.

Conformational consequences of BCL-w$_D$/BAX$_O$ interaction

To interrogate how exposure of BAX$_O$ to BCL-w$_D$ influences its conformation and thus function, we returned to HDX-MS. BAX$_O$ was incubated with excess BCL-w$_D$, and the resulting

Please cite this article in press as: Newman et al., Inhibition of oligomeric BAX by an anti-apoptotic dimer, Cell (2025), https://doi.org/10.1016/j.cell.2025.10.037

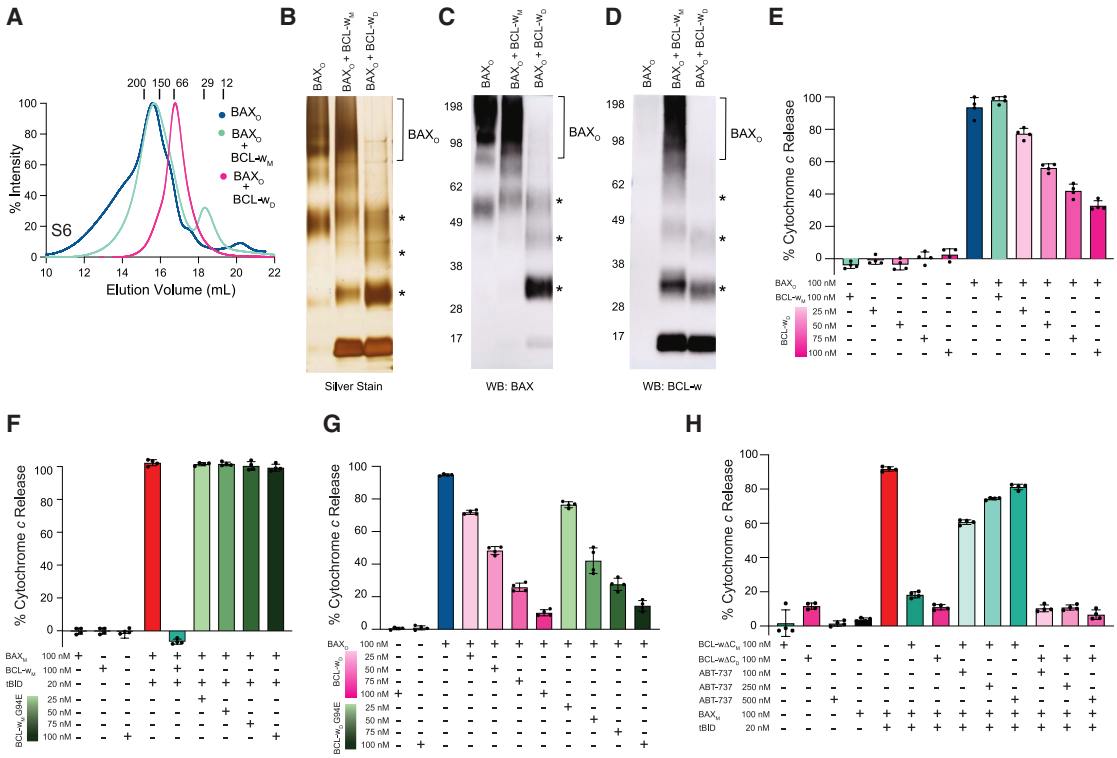

Figure 3. Dimeric BCL-w inhibits BAX oligomerization and function

(A) Higher-order oligomerization of FITC-BAX_O (blue) is essentially unaffected by co-incubation with BCL-w_M (teal) but fully shifted to a lower molecule weight species upon treatment with BCL-w_D (pink).

(B–D) Chemical crosslinking (EDC) of BAX_O alone or in the presence of monomeric or dimeric BCL-w (equimolar BAX and BCL-w based on monomeric content; 3.5 μM each) demonstrates that BCL-w_D eliminates higher-order crosslinked BAX_O bands (B). BAX (C) and BCL-w (D) western analyses showed BAX_O conversion to lower molecular BAX species (asterisks) that contained BCL-w within the crosslinked bands upon incubation with BCL-w_D but not BCL-w_M. Experiments were performed twice using independent protein preparations/reagents with similar results.

(E) BCL-w_D, but not BCL-w_M, inhibits BAX_O-mediated cytochrome *c* release from liver mitochondria isolated from AlbCre^{pos}*Bax*$^{f/f}$*Bak*$^{-/-}$ mice, as measured by ELISA assay. BAX_O, 100 nM; BCL-w_M, 100 nM; BCL-w_D, 25–100 nM.

(F and G) G94E mutagenesis abrogates the capacity of BCL-w_M to block tBID-triggered BAX_M-mediated cytochrome *c* release (F) but does not affect the ability of BCL-w_D to dose-responsively inhibit BAX_O-mediated cytochrome *c* release. BAX_M, 100 nM; tBID, 20 nM; BCL-w_M, 100 nM; BCL-w_M G94E, 25–100 nM; BAX_O, 100 nM; BCL-w_D and BCL-w_D G94E, 25–100 nM.

(H) ABT-737 dose-responsively inhibits BCL-$w_M\Delta C$ blockade of tBID-triggered, BAX_M-mediated cytochrome *c* release but does not disrupt the BAX-suppressive effect of BCL-$w_D\Delta C$. BAX_M, 100 nM; tBID, 20 nM; BCL-$w_M\Delta C$, 100 nM; BCL-$w_D\Delta C$, 100 nM; ABT-737, 100–500 nM.

For mitochondrial experiments, data are mean ± SD for cytochrome *c* ELISA assays performed in technical quadruplicate and repeated twice with independent protein/mitochondrial preparations. BAX_M, BAX_O, BCL-w_M, and BCL-w_D concentrations are based on monomeric protein content.

See also Figure S3.

deuterium exchange profile was compared with that of BAX_O alone. The predominant effect of BCL-w_D was to induce transient deprotection of α1 and persistent deprotection of the α2-α3 hinge, α6, and distal α9 (Figures 4A–4C; Data S1), with the latter regions otherwise buried in oligomeric and membrane-embedded BAX_O[14] (Figures S4A and S4B). Mapping these deprotected regions onto the structure of BAX_O[13] provides fresh insight into how BCL-w_D may disrupt BAX_O through disengaging its repeating units, including α9/α9 interactions between tetramers, α6/α6 interactions between asymmetric dimers, α2/α3 interactions within asymmetric dimers, and membrane-targeting components, such as α6 and α9 (Figure 4C). We next incubated BCL-w_D with excess BAX_O and compared the HDX-MS profile with that of BCL-w_D alone. Upon incubation with BAX_O, BCL-w_D exhibited prominent regions of persistent protection in α1, the α1-α2 loop, and α2 (Figures 4D–4F; Data S1), the regions found to have the highest level of deprotection upon conversion of BCL-w from monomer to dimer (Figures 2A–2C). Further affected areas include prominent protection of the α2-α3 and α4-α5 hinges, α6, and α9, and transient deprotection of proximal α9, all key BCL-w regions implicated in conformational alteration upon dimerization. Intriguingly, these same regions in BAX lie at its dimer-dimer and protein-membrane interfaces (Figures 4C and S4B). Thus, the HDX-MS studies suggest that upon interaction with BAX_O, the very regions that are conformationally exposed upon BCL-w_D formation become engaged and re-protected, resulting in exposure of BAX_O regions implicated in self-association and membrane interaction.[14]

To further explore these findings, we chemically crosslinked BAX_O in the presence of BCL-w_D, focusing first on enriched

Please cite this article in press as: Newman et al., Inhibition of oligomeric BAX by an anti-apoptotic dimer, Cell (2025), https://doi.org/10.1016/j.cell.2025.10.037

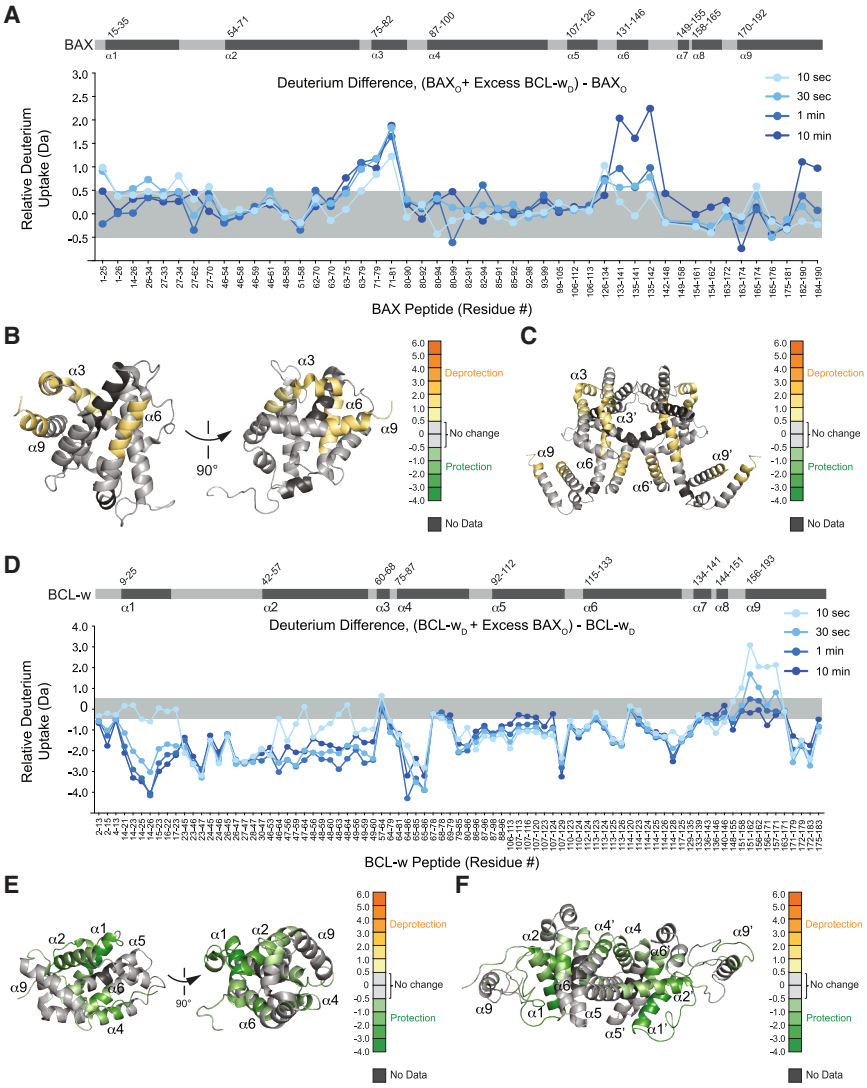

Figure 4. Reciprocal changes in the HDX-MS profiles of BAX$_O$ and BCL-w$_D$ upon interaction

(A–C) Deuterium difference plot showing the relative deuterium incorporation of BAX$_O$ plus excess BCL-w$_D$ minus BAX$_O$ alone in solution (A), with areas of protection and deprotection of BAX$_O$ at 10 min mapped onto BAX$_M$ (PDB: 1F16) (B) and BAX$_O$ (PDB: 9IXU) (C) (significance threshold, ±0.5 Da). Data are representative of at least three biological replicates.

(D–F) Deuterium difference plot showing the relative deuterium incorporation of BCL-w$_D$ plus excess BAX$_O$ minus BCL-w$_D$ alone in solution (D), with areas of protection and deprotection of BCL-w$_D$ at 10 min mapped onto BCL-w$_M$ (PDB: 1O0L) (E) and MD-derived BCL-w$_D$ (F) (significance threshold, ±0.5 Da). Data are representative of two independent biological replicates.

See also Figures S4 and S5 and Data S1.

BAX$_O$ crosslinks arising from exposure to BCL-w$_D$. The majority of induced proximities involved the α1/α1-α2 loop region of BAX, which is unresolved in the BAX$_O$ structure,[13] in addition to crosslinks within the α2-α5 region (Figures S4C–S4E; Table S2; Data S2). These data again suggest that at least a portion of the conformational change in BAX$_O$ upon BCL-w$_D$ engagement results in mobilization of the N-terminal region, consistent with its altered range of interactions.[14] We next searched for intermolecular crosslinks to pinpoint regions of BAX$_O$-BCL-w$_D$ interaction and detected crosslinks between α1 residues of BAX$_O$ and α1, α2-α4, and α9 residues of BCL-w$_D$ (Figure S4F; Table S3; Data S2). The similarity of crosslinked residues enriched in BCL-w$_D$ upon homo-dimerization (Table S1C) and upon exposure to BAX$_O$ (Table S3) suggests potential homology between homo- and hetero-interactions within BCL-w$_D$ and upon BAX$_O$/BCL-w$_D$ engagement, respectively. Specifically, α1 residues of both BAX$_O$ and BCL-w$_D$ crosslink to a subset of identical residues that colocalize on the surface of BCL-w$_D$ (Figures S4F and S4G). Upon oligomer formation, α1 residues of BAX crosslink to a defined cluster of α1-α4 surface residues on BAX$_O$[14] (Figure S4H). These findings suggest that the α1 motifs of BCL-w$_D$ and BAX$_O$ constitutively engage binding sites on their respective protein surfaces, but upon exposure to one another, they may engage in reciprocal competitive interactions that alter their conformations and promotes BAX$_O$ dissociation.

To probe this hypothesis of competitive binding sites that involve α1 interaction, we generated a fluorescently labeled, stapled alpha-helix of BAX α1 (FITC-SAH-BAX$_{α1}$) and measured its binding interactions with BCL-w$_M$ and BCL-w$_D$ by fluorescence polarization (FP) binding analyses. We observed that SAH-BAX$_{α1}$ bound to BCL-w$_D$ with an EC$_{50}$ of 130 nM but showed little to no interaction with BCL-w$_M$ (Figure S5A). To examine the conformational consequences of binding, we compared the HDX-MS profiles of BCL-w$_D$ in the presence and absence of SAH-BAX$_{α1}$ and observed deprotection of the N-terminal region, including α1, the α2-α3 hinge, and proximal α9, and protection of distal α9, areas that are in unique proximity to one another in the MD-derived structure of BCL-w$_D$ (Figures S5B and S5C). These HDX-MS findings are consistent with the stapled peptide displacing the endogenous α1, resulting in its deprotection and conformational perturbation of the adjacent α2-α3 hinge and α9 helix. Notably, these areas of conformational alteration colocalize with the cluster of crosslinks observed between the endogenous BCL-w α1 and BCL-w$_D$ (Figure S5D). We then performed the converse experiment, evaluating the binding activity of FITC-SAH-BCL-w$_{α1}$ for BAX. Again, the stapled peptide demonstrated binding specificity for BAX$_O$

(EC_{50}, 266 nM) over BAX_M (Figure S5E). In the corresponding HDX-MS analysis, engagement of BAX_O by BCL-$w_{\alpha1}$ caused prominent protection of the α1/α2 region, the very site of enriched crosslinks to endogenous α1 upon BAX_O formation[14] (Figures S5F–S5H). Protection of α6 and the C-terminal region, albeit less prominent, was also observed, which could reflect allosteric changes in BAX_O upon FITC-SAH-BCL-$w_{\alpha1}$ binding to the α1/α2 region. To test the functional relevance of BCL-w_D and BAX_O α1s in mediating BAX_O inhibition, we assessed the impact of N-terminal deletion of each protein, individually and in combination, on mitochondrial cytochrome *c* release. Whereas deletion of either N terminus alone only modestly reduced BAX_O inhibition, with BCL-w_D truncation having a greater effect than BAX_O truncation, deletion of both N termini markedly impaired inhibition. Indeed, dual deletion restored a significant portion of $BAX_O\Delta N$'s membrane-permeabilizing activity (Figure S5I), pointing to a reciprocal mechanism of regulation involving the N termini of BCL-w_D and BAX_O.

Reversal of BAX_O-induced disruptive membrane curvature by BCL-w_D

Our biochemical and structural data implicate a mechanistic role of direct protein-protein interaction in BCL-w_D inhibition of BAX_O. Because the "execution phase" of BAX-mediated apoptosis occurs in the MOM, we next investigated how these higher-order species of BCL-w and BAX interact with the membrane itself to influence the poration functionality of BAX_O. The local shape at any given point on a membrane surface is characterized by its two orthogonal principal curvatures, c_1 and c_2, which are used to describe general deformations of a membrane surface by two general expressions: the mean curvature, $H = \frac{1}{2}(c_1 + c_2)$, and the Gaussian curvature, $K = c_1c_2$. For a flat surface, both principal curvatures are zero, such that $H = 0$ and $K = 0$; for a dome-shaped surface, both principal curvatures are positive, and therefore $H > 0$ and $K > 0$; and for a saddle-shaped surface that is convex in one direction and concave in the other, c_1 and c_2 have opposite signs, resulting in negative Gaussian curvature (NGC) (Figure 5A). NGC is a geometric requirement for a variety of membrane-destabilizing processes, including the formation of transmembrane pores during mitochondrial apoptosis.[26–28] By contrast, the induction of positive Gaussian curvature (PGC) can inhibit membrane-permeating activity by counteracting NGC.[29]

With these principles in mind, we applied SAXS to examine the effect of BAX_O on membrane curvature. SAXS demonstrated that BAX_O restructured lipid vesicles into bicontinuous cubic phases rich in NGC (Figures 5B and 5C), facilitating the saddle-shaped membrane deformation modes required to form stable transmembrane pores. We observed a coexistence of two cubic phases: (1) a *Pn3m* cubic phase (q ratios $\sqrt{2}:\sqrt{3}:\sqrt{4}:\sqrt{6}$) with a lattice constant of a_{Pn3m} = 20.7 nm and (2) an *Im3m* cubic phase (q ratios $\sqrt{2}:\sqrt{4}:\sqrt{6}:\sqrt{8}:\sqrt{10}:\sqrt{12}$) with a lattice constant of a_{Im3m} = 26.3 nm (Figure 5B). The coexistence of *Pn3m* and *Im3m* cubic phases in the system, with a ratio of lattice parameters close to the Bonnet ratio of 1.279,[30] indicates that the system is near equilibrium and the induced NGC is balanced. The average amount of Gaussian curvature, *K*, in a cubic phase can be calculated using the equation $\langle K \rangle = 2\pi\chi/A_0a^2$, where *a* is the lattice parameter, and χ and A_0 are constants specific to each cubic phase.[31,32] Using the lattice constants of *Pn3m* and *Im3m*, we calculated that BAX_O can induce $\langle K \rangle = -0.015\ nm^{-2}$ on the membrane (Figure 5B). Strikingly, co-treatment with BCL-w_D dose-responsively reversed the membrane-disruptive NGC induction by BAX_O (Figure 5D). Specifically, we kept the protein-to-lipid (*P/L*) molar ratio of BAX_O constant and increased the (*P/L*) molar ratio of X = BCL-w_D/BAX_O from X = 0 to X = 2 (Figure 5D). The addition of BCL-w_D, but not BCL-w_M, induced drastic suppression of all cubic phases, even at a molar ratio of X = 0.25 (Figures 5D and S6A). As the concentration of BCL-w_D increased, a lamellar phase with zero mean and Gaussian curvature was formed (Figure 5D).

To investigate the mechanistic basis of BCL-w_D's neutralizing activity, we tested whether BCL-w_D was capable of independently inducing PGC on membranes. A model membrane composed of 100% phosphatidylethanolamine (PE) lipids can form an inverted hexagonal phase with no NGC (q ratios $\sqrt{1}:\sqrt{3}:\sqrt{4}:\sqrt{7}$ with $a_{hexagonal}$ = 7.4 nm corresponding to $H = -0.067\ nm^{-1}$) and cubic phases rich in NGC (a_{Pn3m} = 13.9 nm and a_{Im3m} = 17.4 nm corresponding to $\langle K \rangle = -0.034\ nm^{-2}$) (Figure 5E). The addition of BCL-w_D completely eliminated all cubic diffraction peaks and ablated the cubic phase (Figures 5E and 5F) in a manner consistent with BCL-w_D's turn-off of cubic phases induced by BAX_O. These data indicate that in addition to the impact of BCL-w_D interaction on the oligomeric state of BAX, the proximity of BCL-w_D to BAX_O in the membrane context has a direct effect on the curvature of the membrane itself, neutralizing BAX_O-mediated NGC that otherwise induces permeabilization.

Dimeric BCL-w blocks mitochondrial translocation of BAX_O and induces its retrotranslocation

Given the direct influence of BCL-w_D on BAX_O and the curvature of the membrane, the very target of BAX function, we sought to understand the mechanistic implications of the SAXS data at the level of the mitochondria. We developed an assay system whereby BAX_O or BCL-w_D is incubated with mitochondria purified from the livers of $AlbCre^{pos}Bax^{f/f}Bak^{-/-}$ mice, followed by isolation and resuspension of the pellet. Then, the mitochondria pretreated with BAX_O or BCL-w_D are exposed to increasing doses of added BCL-w_D or BAX_O, respectively, followed by isolation of the supernatant and pellet, which are analyzed by electrophoresis and western blotting (Figure 6A). As we previously reported,[14] BAX_O autotranslocates to mitochondria, evidenced by its presence in the pellet (Figure 6B). As the dose of BCL-w_D was increased, BAX relocated from the mitochondrial pellet to the supernatant, with near-total retrotranslocation at a 4:1 ratio (based on monomeric content) of BCL-w_D to BAX_O, as added at the preloading step (Figure 6B). Probing for BCL-w revealed that, initially, BCL-w_D translocated to the pellet, but starting at the doses that induced BAX retrotranslocation (2:1 BCL-w_D/BAX_O), the mitochondrial localization of BCL-w began to decrease (Figure 6C). At the 4:1 ratio of BCL-w_D/BAX_O, BCL-w_D was predominantly localized in the supernatant, whereas at the same 4:1 ratio, BCL-w_M partitioned relatively equally between the two fractions and did not retrotranslocate BAX (Figure 6C). These data indicate that the dimer, rather

Please cite this article in press as: Newman et al., Inhibition of oligomeric BAX by an anti-apoptotic dimer, Cell (2025), https://doi.org/10.1016/j.cell.2025.10.037

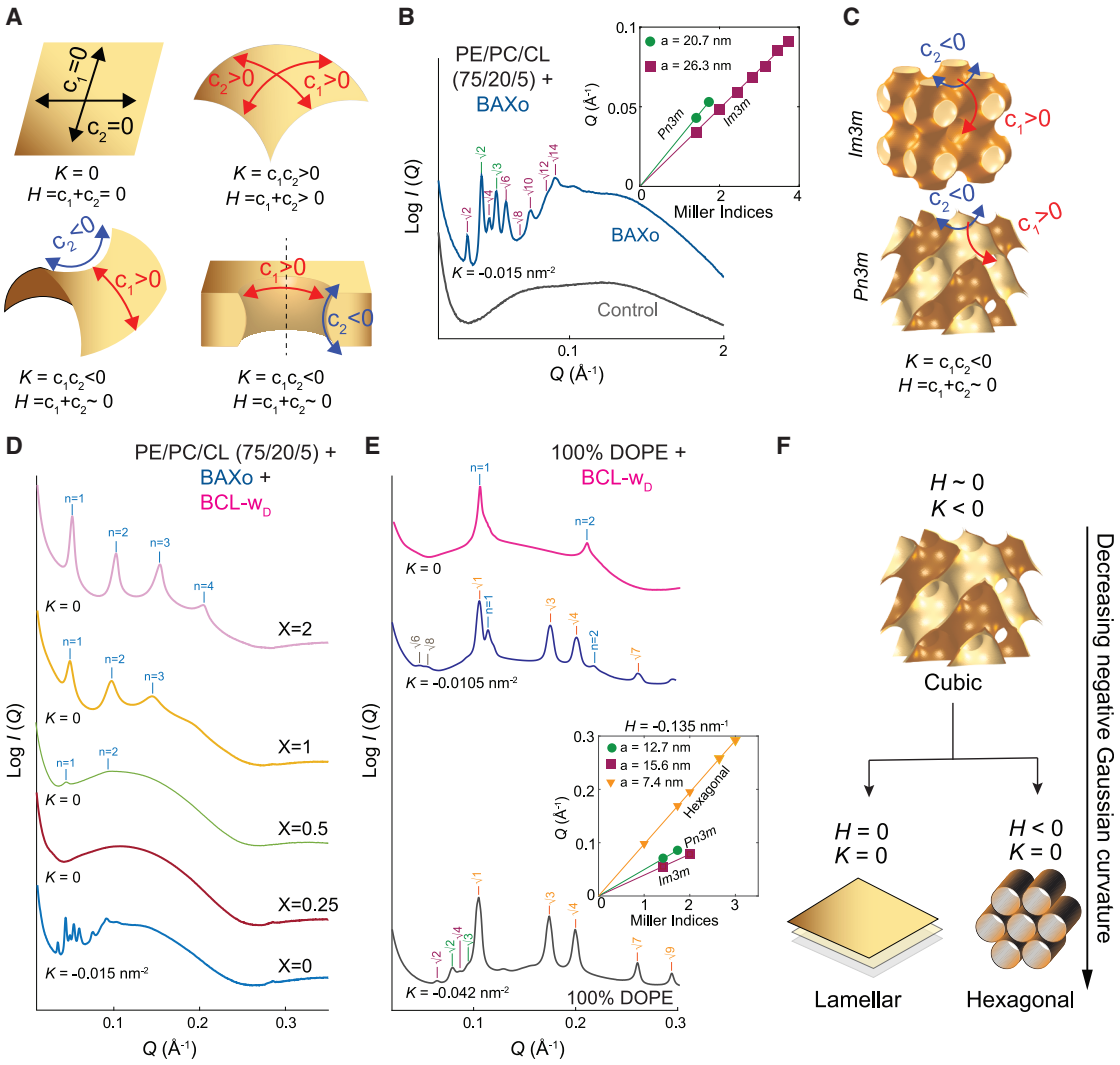

Figure 5. BCL-w_D neutralizes the disruptive effect of BAX_O on membrane curvature

(A) Schematic of flat (upper left), dome-shaped (upper right), and saddle-shaped (bottom left) surfaces that contribute to the formation of transmembrane pores (bottom right), reflecting zero, positive, and negative Gaussian curvatures.

(B) SAXS spectra of model membranes (small unilamellar vesicles [SUVs]) containing phosphatidylethanolamine (PE), phosphatidylcholine (PC), and cardiolipin (CL) at a PE/PC/CL ratio of 75/20/5 alone (black) and upon incubation with BAX_O (0.476 g/L) at a protein-to-lipid ratio (P/L) of 1/3,500 (blue). The insert shows plots of measured Q positions versus assigned reflections as Miller indices $\sqrt{h^2+k^2+l^2}$ for cubic phases. Lattice parameters were calculated from slopes of linear regressions.

(C) *Pn3m* and *Im3m* cubic phases generated by BAX_O, with features of predominant NGC.

(D) SAXS spectra of PE/PC/CL 75/20/5 SUVs incubated with BAX_O alone or with increasing amounts of BCL-w_D (X = BCL-w_D:BAX_O molar ratio based on monomeric protein), demonstrating dose-responsive blockade of BAX_O-induced NGC. BAX_O, 0.476 g/L; BCL-w_D, X = 0.25, 0.119 g/L; X = 0.5, 0.238 g/L; X = 1, 0.476 g/L; X = 2, 0.952 g/L.

(E) SAXS spectra of 100% PE model membrane (black) demonstrate the inherent inverse hexagonal phase with a negative mean curvature of $H = -0.067\ nm^{-1}$ and bicontinuous cubic phase reflective of NGC ($\langle K \rangle = -0.034\ nm^{-2}$). Addition of BCL-$w_D$ (blue, 0.2 g/L; pink, 0.4 g/L) dose-responsively suppresses negative mean curvature and NGC by inducing PGC and formation of a lamellar phase.

(F) Schematic of structures classified by SAXS, including cubic, hexagonal, and lamellar phases, which reflect the progressive reduction of membrane curvature.

than the monomer, of BCL-w is the species that retrotranslocates mitochondrial BAX_O.

We next examined whether preloading mitochondria with BCL-w_D could block BAX_O translocation from supernatant to mitochondria. As a control for this reverse experiment, we demonstrated that BAX_O dose-responsively translocated to the pellet of untreated mitochondria (Figure 6D). However, when the mitochondria were preloaded with BCL-w_D, BAX_O translocation was blocked, with the inhibitory effect of BCL-w_D only starting to be overcome at a 4:1 excess of BAX_O (Figure 6E). In contrast to the retrotranslocation context, levels of BCL-w in the supernatant and mitochondrial pellet were constant across

Please cite this article in press as: Newman et al., Inhibition of oligomeric BAX by an anti-apoptotic dimer, Cell (2025), https://doi.org/10.1016/j.cell.2025.10.037

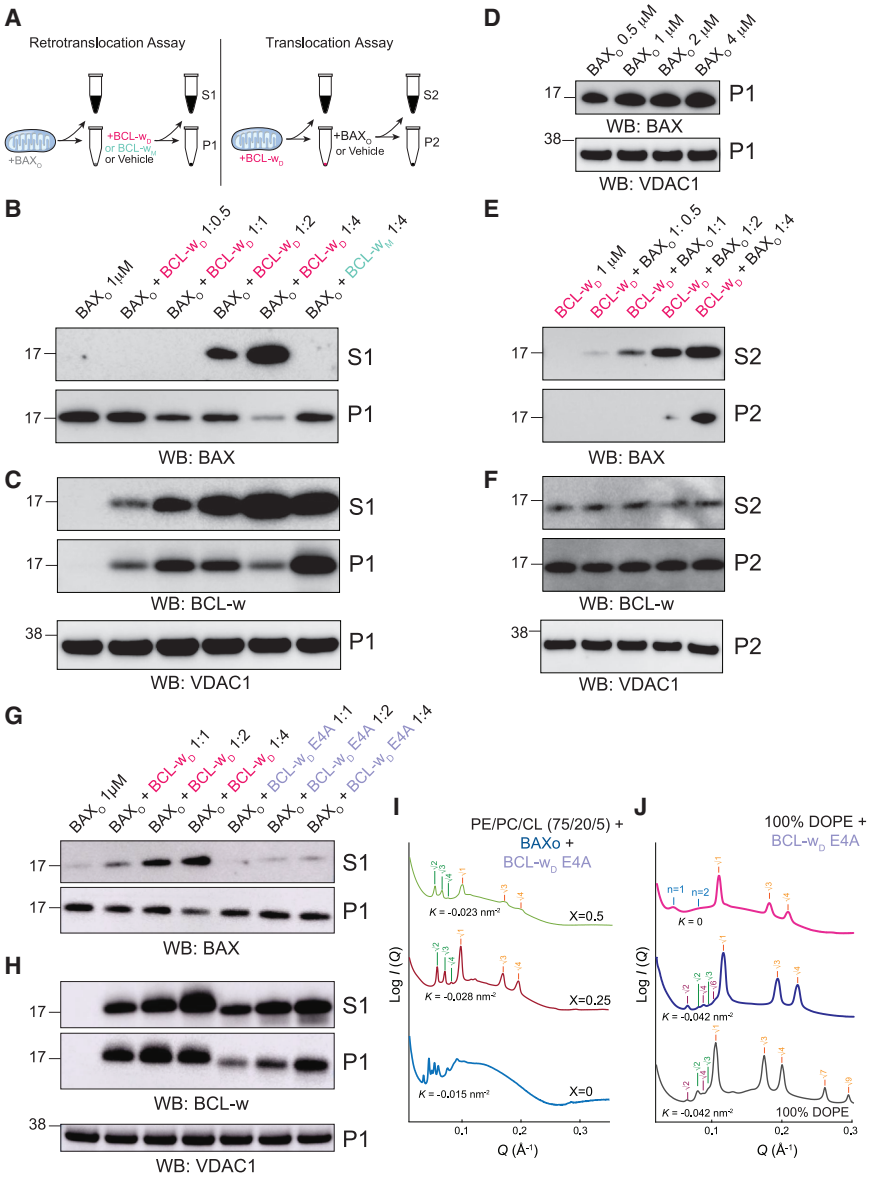

Figure 6. BCL-w_D inhibits BAX_O through protein and membrane interaction, blocking mitochondrial translocation and inducing retrotranslocation

(A) Workflow for mitochondrial retrotranslocation (left) and translocation (right) assays.

(B and C) Preincubation of BAX/BAK-deficient mitochondria with BAX_O (1 μM) followed by isolation of the mitochondrial pellet demonstrates autotranslocation, as detected by BAX western blot of the electrophoresed samples (B). Treatment of BAX_O-containing mitochondria with increasing doses of BCL-w_D (0.5–4 μM) leads to retrotranslocation of BAX from mitochondria to supernatant (B). Whereas BCL-w_D initially and dose-responsively translocates to the mitochondrial pellet, starting at the same dosing ratio that produces retrotranslocation of BAX (1:2 BAX_O:BCL-w_D), BCL-w_D shifts to being predominantly in the supernatant rather than pellet (C). Applying the same concentration of BCL-w protein that produces maximal BAX translocation by BCL-w_D, BCL-w_M exhibits no BAX retrotranslocation activity and partitions relatively equally between supernatant and pellet (C). Voltage-dependent anion channel 1 (VDAC1) was used as a mitochondrial marker and loading control.

(D) BAX/BAK-deficient mitochondria treated with increasing concentrations of BAX_O (0.5–4 μM) demonstrate dose-responsive autotranslocation of BAX_O to mitochondria, as detected by BAX western blot of the pellet fraction.

(E and F) Pretreatment of mitochondria with BCL-w_D (1 μM), followed by re-isolation of mitochondria and treatment with BAX_O (0.5–4 μM), revealed blockade of BAX_O translocation (E). BCL-w western analysis of supernatant and pellet fractions demonstrated that BCL-w_D partitioning between supernatant and pellet fractions remained constant across BCL-w_D:BAX_O treatment ratios (F).

(G and H) E109A/E114A/E116A/E124A (E4A) mutagenesis of BCL-w impairs the capacity of BCL-w_D (1–4 μM) to retrotranslocate BAX_O (1 μM) from mitochondria.

(I) The capacity of BCL-w_D to dose-responsively negate BAX_O-induced NGC is impaired upon E4A mutagenesis, as evaluated by SAXS spectra of PE/PC/CL 75/20/5 SUVs incubated with BAX_O alone or in combination with increasing amounts of BCL-w_D E4A (X = BCL-w_D:BAX_O molar ratio based on monomeric protein). BAX_O, 0.476 g/L; BCL-w_D E4A, X = 0.25, 0.119 g/L; X = 0.5, 0.238 g/L.

(J) BCL-w_D E4A exhibits impaired induction of PGC compared with BCL-w_D WT (Figure 5E), as measured by SAXS spectra of 100% PE model membrane in the absence (black) and presence of increasing amounts of BCL-w_D E4A (blue, 0.2 g/L; pink trace, 0.4 g/L).

Mitochondrial experiments were performed twice using independent protein/mitochondrial preparations with similar results.

See also Figures S6 and S7.

BAX_O:BCL-w_D ratios, with BCL-w remaining in the mitochondria throughout (Figure 6F). Finally, we asked whether the dimer-dependent activities observed for BCL-w are relevant to other anti-apoptotic proteins. We found that full-length BCL-X_L also undergoes Fos-14-induced dimerization as monitored by SEC (Figure S6B) and that BCL-X_{LD}, but not BCL-X_{LM}, dose-responsively blocks BAX_O-mediated cytochrome *c* release (Figure S6C) and induces BAX_O retrotranslocation from mitochondria (Figure S6D). Taken together, the SAXS and mitochondrial data suggest that the capacity of BCL-w_D to induce PGC in membranes likely contributes both to preventing BAX_O from translocating to mitochondria that contain BCL-w_D and inducing the retrotranslocation of mitochondrial BAX_O. We further find that BCL-w_D, rather than BCL-w_M, is the active anti-apoptotic species involved in BAX_O retrotranslocation.

Mutagenesis of the membrane-regulatory region of BCL-w_D impairs anti-apoptotic function in cells

To further validate our mechanistic conclusions in cells, we sought to identify mutants that would prevent BCL-w_D from exerting its membrane-modifying effects. We previously reported that the α6 region of BAX is composed of hydrophobic and positively

Please cite this article in press as: Newman et al., Inhibition of oligomeric BAX by an anti-apoptotic dimer, Cell (2025), https://doi.org/10.1016/j.cell.2025.10.037

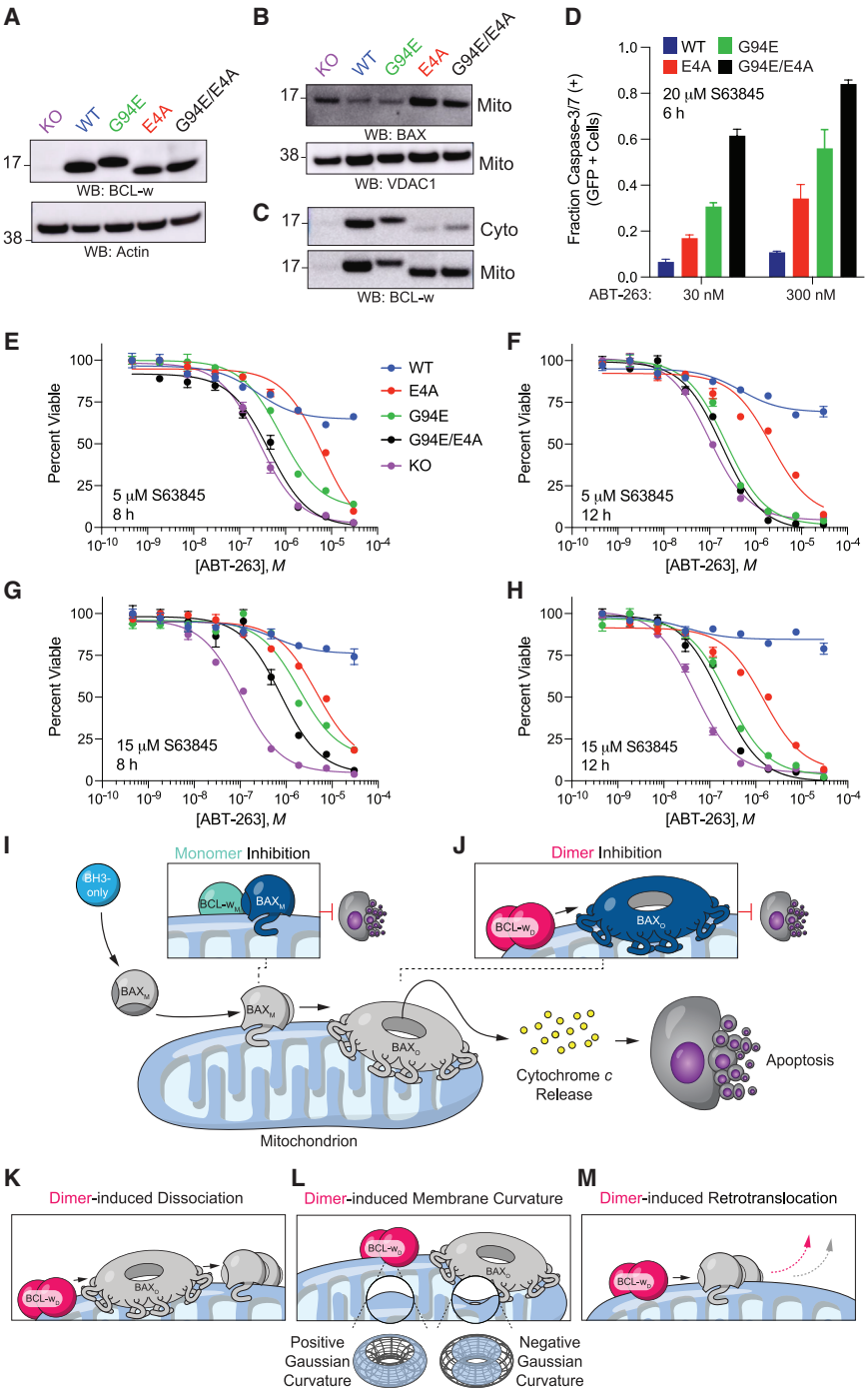

Figure 7. Dissection of the canonical and non-canonical anti-apoptotic activities of BCL-w in cells

(A) BCL-w western blot of lysates from *Bcl-w*$^{-/-}$ MEFs and those reconstituted with WT, E4A, G94E, or G94E/E4A BCL-w protein.

(B and C) BAX western blot of the mitochondrial fraction isolated from MEF lysates, demonstrating relatively increased levels of mitochondrial BAX upon E4A mutagenesis (alone or with G94E), as compared with WT and G94E specimens (B). E4A mutagenesis increases BCL-w partitioning to mitochondrial pellet relative to cytosol (C). Experiments were performed twice using independent cell preparations with similar results.

(D) Combination treatment with ABT-263 (30, 300 nM) and S63845 (20 μM) caused a progressive increase in GFP-positive cells exhibiting caspase-3/7 activation as measured by ImageXpress Micro (IXM) high-content imaging at 6 h for MEFs reconstituted with BCL-w WT, E4A, G94E, or G94E/E4A. Data are mean ± SD for experiments performed in technical quadruplicate and repeated twice with independent compound/cell preparations.

(E–H) Cell viability of *Bcl-w*$^{-/-}$ MEFs and those reconstituted with WT, E4A, G94E, or G94E/E4A BCL-w in response to treatment with the indicated serial dilution of ABT-263 combined with 5 μM S63845 at 8 h (E) and 12 h (F), or 15 μM S63845 at 8 h (G) and 12 h (H). Data are mean ± SD for experiments performed in technical quadruplicate and repeated twice with independent compound/cell preparations.

(I–M) Canonical mode of inhibiting BAX-mediated apoptosis, as mediated by heterodimeric interaction between BCL-w and activated BAX monomers (I). Inhibition of BAX_O by dimeric BCL-w (J), which induces BAX_O dissociation (K), PGC that counterbalances BAX_O-mediated NGC (L), and BAX_O retrotranslocation (M).

charged residues, resembling antimicrobial peptides that induce plasma membrane rupture.[14] Intriguingly, 70% of electrostatic residues in the α5-α6 region of BAX are positively charged, whereas 71% in BCL-w are negatively charged (Figures S7A and S7B), leading us to hypothesize that these negatively charged residues are critical for the induction of PGC in the membrane. Thus, we generated a BCL-w E109A/E114A/E116A/E124A quadruple mutant (hereafter referred to as BCL-w E4A) and confirmed that BCL-w_M E4A retained BH3-binding activity—inhibiting tBID-triggered, BAX-mediated cytochrome *c* release (Figure S7C)—and the ability to dimerize (Figure S7D). However, BCL-w_D E4A was notably impaired in blocking BAX_O-mediated cytochrome *c* release and BAX_O retrotranslocation (Figures 6G, 6H, and S7E). BCL-w_D E4A also failed to reverse the NGC induced by BAX_O or independently induce PGC, as evaluated by SAXS (Figures 6I and 6J).

With mutants to selectively probe the canonical and non-canonical functionalities of BCL-w in hand, we reconstituted *Bcl-w*$^{-/-}$ mouse embryonic fibroblasts (KO MEFs) with BCL-w WT and a series of mutant constructs, including BCL-w E4A, G94E, and G94E/E4A (Figure 7A), and evaluated their relative influence on mitochondrial BAX levels (Figure 7B). We observed that E4A mutagenesis, whether alone or in combination with

Please cite this article in press as: Newman et al., Inhibition of oligomeric BAX by an anti-apoptotic dimer, Cell (2025), https://doi.org/10.1016/j.cell.2025.10.037

BCL-w G94E, resulted in increased mitochondrial levels of BAX as compared with WT or G94E BCL-w (Figure 7B). Like E4A mutagenesis, BCL-w KO also exhibited elevated mitochondrial levels of BAX relative to MEFs reconstituted with BCL-w WT or G94E. These data are consistent with relative loss of BAX retrotranslocation upon selective mutagenesis of the membrane-altering feature of BCL-w. In alignment with this interpretation, the relative partitioning of BCL-w to the mitochondria was increased upon E4A mutagenesis (Figure 7C). These data corroborate our *in vitro* observations, whereby the mitochondrial levels of BCL-w_D decreased in concert with BAX retrotranslocation but accumulated in the mitochondria upon E4A mutagenesis, which caused marked impairment of BAX retrotranslocation (Figures 6B, 6C, 6G, and 6H).

To evaluate the relative impact of BCL-w's canonical and non-canonical functions on apoptosis induction, we compared caspase-3/7 activation upon combined treatment with the anti-apoptotic BCL-2 protein inhibitors ABT-263[33] and S63845.[34] We observed progressively impaired anti-apoptotic function of reconstituted BCL-w upon E4A, G94E, and G94E/E4A mutagenesis, as reflected by increasing caspase-3/7 positivity among the corresponding GFP-positive cells (Figure 7D). In assessing comparative cell viability responses, reconstitution with BCL-w WT effectively rescued MEFs from the ABT-263/S63845 combination, whereas the E4A, G94E, and G94E/E4A mutants again showed progressive impairment of anti-apoptotic function, with combined disruption of canonical (G94E) and non-canonical (E4A) functions found to be as impaired as the KO (Figure 7E). The relative disruption of rescue by the E4A mutant as compared with WT persisted over time, with the distinctions between G94E and G94E/E4A mutants becoming less apparent and mirroring the response of KO MEFs (Figure 7F). Tripling the dose of S63845 in the drug combination increased the death response for KO MEFs and again revealed the progression in impaired rescue for the E4A, G94E, and G94E/E4A mutants (Figure 7G). Similar to the lower dosing regimen, monitoring over time revealed the increased death response for KO MEFs, a decrease in the distinction between G94E and G94E/E4A activities, and persistence of the rescue defect upon E4A mutagenesis as compared with WT (Figure 7H). These cellular data suggest that the non-canonical, membrane-altering activity of BCL-w not only regulates the constitutive level of BAX at the mitochondria during homeostasis but also influences cellular fate upon apoptosis induction, most prominently during the early phase of cell stress.

DISCUSSION

The commitment step of mitochondrial apoptosis has been framed as a duel between activated BAX/BAK and anti-apoptotic monomers (Figure 7I). This "BH3-in-groove" paradigm is structurally defined and clinically leveraged yet does not account for whether higher-order anti-apoptotic assemblies exist, how they might intersect with BAX oligomers, or how proteins with such similar folds exert diametrically opposed functions. Here, we identify and characterize a full-length, symmetric dimer of BCL-w that operates downstream of BH3 sequestration to dismantle and retrotranslocate oligomeric BAX and help preserve mitochondrial integrity (Figure 7J).

Biophysical and structural analyses converged on a distinctive architecture for BCL-w_D. SEC-MALS and SEC-SAXS establish a ~41–48 kDa dimer with an elongated, symmetric envelope featuring a compact central core and outward-projecting elements. A structural model depicts the α3-α4 hairpin from each protomer engaged with the contralateral α5-α6 hairpin, generating a globular core, and the N- and C-terminal segments positioned outward for accessibility. HDX-MS corroborated a major conformational rearrangement upon dimerization, with exposure of the N-terminal region alongside changes across α3-α6 and α7-α9, consistent with the model. Truncation mapping defined α2-α8 as the minimal self-association unit, with α7-α8 identified as a determinant of dimer formation.

Against the backdrop of the BAX oligomer structure[13]—an array of asymmetric α2-α9 dimers that tetramerize into repeating units—BCL-w_D directly disrupts higher-order BAX (Figure 7K). FSEC and crosslinking showed that BCL-w_D, but not BCL-w_M, converts BAX_O into lower-order species. HDX-MS mapped the conformational consequences: in BAX, BCL-w_D induces deprotection of α1, the α2-α3 hinge, α6, and distal α9, elements that mediate dimer-dimer contacts, membrane insertion, and inter-tetramer connectivity in the oligomer. Reciprocally, the N-terminal regions of BCL-w that become exposed during dimerization become protected upon BAX_O engagement, indicating formation of an interface that disfavors oligomer maintenance. Crosslinking localized intermolecular contacts to α1 residues in both partners and revealed homology between crosslinked residues enriched during BCL-w homo-dimerization and those engaged upon BAX_O binding, supporting a competitive-interface model. BCL-w_D α9 helices are poised to compete with BAX α9 interactions that support homo-oligomerization.

Membrane mechanics add a cooperative layer of control, linking the contrasting functions of pro- and anti-apoptotic proteins to opposing effects on membrane curvature. SAXS on lipid systems showed that BAX_O induces NGC, whereas BCL-w_D imposes PGC, extinguishing the NGC of BAX_O (Figure 7L). At mitochondria, these opposing properties manifest as functional outcomes: BCL-w_D blocks BAX_O translocation and retrotranslocates prebound BAX_O back to the soluble fraction (Figure 7M). The effect depends on negatively charged amphipathic segments within the α5-α6 hairpins, which, in the context of BCL-w_D, are symmetrically positioned for membrane engagement. An E109A/E114A/E116A/E124A-mutant BCL-w monomer retains BH3-groove binding and self-association, but the corresponding dimer loses curvature remodeling, retrotranslocation, BAX_O inhibition, and the capacity to fully rescue MEFs upon apoptosis induction. Thus, BCL-w_D integrates protein-protein competition with membrane-curvature reprogramming to dismantle the BAX lattice and reduce insertion competence of its α6 and α9 regions.

Notably, these dimer-specific activities are independent of the canonical groove. Neither G94E mutagenesis nor ABT-737 disrupt BCL-w dimerization or BCL-w_D-specific suppression of BAX_O. BCL-X_L likewise forms a detergent-induced dimer that inhibits BAX_O and drives retrotranslocation, suggesting that anti-apoptotic dimers may represent a conserved regulatory class.

Our results reposition anti-apoptotic proteins as active regulators of the oligomeric execution machinery at the membrane, rather than monomeric sequestrants alone. Cellular analyses dissected distinct contributions of these canonical and non-canonical modalities in regulating apoptosis.

Our findings add a downstream tier to the central dogma of BCL-2 family control. Upstream, anti-apoptotic monomers prevent the consequences of BAX activation by BH3 capture, and downstream, dimers oppose oligomeric BAX by contesting its interfaces and reversing its membrane curvature, raising the threshold for apoptosis by shuttling BAX away from the MOM. Because the monomeric and dimeric activities rely on non-overlapping structural determinants, they offer orthogonal therapeutic entry points. Agents that disable anti-apoptotic dimers or blunt their membrane-curvature remodeling could complement BH3-mimetics to intensify tumor cell killing, whereas strategies that stabilize dimers or enhance PGC may be protective where pathological apoptosis predominates.

Limitations of the study

Our dimer model integrates SEC-SAXS, HDX-MS, crosslinking MS, and MD to define a symmetric architecture and map functional interfaces, but atomic-resolution details await high-resolution structures of BCL-w_D. Although we demonstrate reciprocal conformational changes and functional dismantling of BAX_O, the stoichiometry, kinetics, and persistence of BCL-w_D-BAX_O engagement remain to be quantified with real-time approaches. Disentangling the sequence and sufficiency of protein-protein and protein-membrane contributions within the cellular environment is especially challenging. Selective mutants that prevent dimerization, disrupt the BAX interface, or attenuate membrane curvature as deployed here will continue to discern between alternative modes of apoptotic regulation. The physiological triggers and locales that influence the dimer-monomer balance, including cytosol versus mitochondria, membrane composition, cellular stresses, and post-translational modifications, remain to be established. BCL-2 family redundancy and dynamic co-expression can complicate cellular interpretation. While BCL-w mirrors key dimer-dependent behaviors, a comprehensive map of which anti-apoptotic dimers form in which contexts and their relative contributions to BAX/BAK control during homeostasis and apoptosis induction also requires further investigation. Finally, the translational tractability of modulating dimerization or membrane curvature awaits drug-like probes. Importantly, we view these limitations as invitations. Just as one of our inter-monomeric BAX_O crosslinks defied the α2-α5 dimer structure[14,18] but now precisely maps to an inter-dimer contact in the elucidated BAX tetramer,[13] each advance in structure and mechanism will continue to reconcile the past and refine the models ahead.

RESOURCE AVAILABILITY

Lead contact

Further information and requests for reagents should be directed to the lead contact, Loren Walensky (loren_walensky@dfci.harvard.edu).

Materials availability

Plasmids, stapled peptides, and cell lines are available upon request to the lead contact.

Data and code availability

Data supporting the study's findings are available within the article and its supplemental materials. Proteomic datasets were submitted to the ProteomeXchange Consortium via PRIDE[35] identifier PXD049315.

ACKNOWLEDGMENTS

We thank E. Smith for figure preparation, J. Byrnes and S. Chodankar for SAXS assistance (NIH), J. Champagne for SEC-MALS support, and J. Opferman for p185+ *Arf*$^{-/-}$ cells. This work was funded by NIH grants R35CA197583 to L.D.W., T32GM144273 and F30CA264846 to C.E.N., F31CA210592 to E.P.H., F31CA210590 to Z.J.H., F30CA275293 to E.Y., R50CA211399 to G.H.B., R01GM67945 to S.P.G., T32HL069766 to H.A., and S10OD012331 to L.F. Additional support was provided by NSF grant DMR-2325840 and AHA grant 966662 to G.C.L.W. and a William Lawrence and Blanche Hughes Foundation grant to L.D.W. SAXS experiments performed at the NCI SAXS Facility are supported by the Frederick National Laboratory (75N91019D00024) and the NIH Intramural Research Program. Data were collected at the LiX beamline of CBMS, supported by NIH/NIGMS (P30GM133893) and DOE (KP1605010 and DE-SC0012704).

AUTHOR CONTRIBUTIONS

C.E.N., M.A.G., and L.D.W. conceived of and designed the study. E.P.H. and Z.J.H. contributed to foundational experiments. C.E.N. and M.A.G. performed biochemical experiments assisted by T.M.D., J.G., E.Y., and A.M.C. C.M.C. conducted MD. C.E.N., T.M.D., T.E.W., and J.R.E. performed HDX-MS. J.M. and S.P.G. conducted MS. L.F. and Y.-X.W. undertook SAXS (solution). H.A., E.W.-C.L., and G.C.L.W. designed/performed/analyzed SAXS experiments (membranes). M.A.G., M.G., and G.H.B. executed cellular experiments. L.D.W. wrote and co-authors reviewed the manuscript.

DECLARATION OF INTERESTS

The authors report no competing interests.

STAR★METHODS

Detailed methods are provided in the online version of this paper and include the following:

- KEY RESOURCES TABLE
- EXPERIMENTAL MODEL AND SUBJECT DETAILS
  - Mouse Liver Mitochondria
- METHOD DETAILS
  - Recombinant Protein Expression and Purification
  - Preparation of BAX Oligomers and BCL-w Dimers
  - Analysis of BAX and BCL-w Proteins by Size Exclusion Chromatography
  - Multi-Angle Light Scattering
  - Assessment of BCL-w Dimerization in Cells
  - Small Angle X-ray Scattering Analysis of Dimeric BCL-w
  - Molecular Dynamics Simulation
  - Peptide Synthesis
  - Fluorescence Polarization Binding Assays
  - Hydrogen Deuterium Exchange Mass Spectrometry
  - Preparation of Liposomes
  - Chemical Crosslinking and Mass Spectrometry Analysis
  - Membrane Curvature Analyses by Small Angle X-ray Scattering
  - Mitochondrial Cytochrome *c* Release Assays
  - Mitochondrial Translocation and Retrotranslocation Assays
  - Cellular Analysis of Reconstituted MEFs
- QUANTIFICATION AND STATISTICAL ANALYSIS

SUPPLEMENTAL INFORMATION

Supplemental information can be found online at https://doi.org/10.1016/j.cell.2025.10.037.

Received: February 14, 2024
Revised: August 22, 2025
Accepted: October 29, 2025

REFERENCES

1. Fuchs, Y., and Steller, H. (2011). Programmed cell death in animal development and disease. Cell *147*, 742–758. https://doi.org/10.1016/j.cell.2011.10.033.
2. Korsmeyer, S.J., Wei, M.C., Saito, M., Weiler, S., Oh, K.J., and Schlesinger, P.H. (2000). Pro-apoptotic cascade activates BID, which oligomerizes BAK or BAX into pores that result in the release of cytochrome c. Cell Death Differ. *7*, 1166–1173. https://doi.org/10.1038/sj.cdd.4400783.
3. Cosentino, K., and García-Sáez, A.J. (2017). Bax and Bak Pores: Are We Closing the Circle? Trends Cell Biol. *27*, 266–275. https://doi.org/10.1016/j.tcb.2016.11.004.
4. Sattler, M., Liang, H., Nettesheim, D., Meadows, R.P., Harlan, J.E., Eberstadt, M., Yoon, H.S., Shuker, S.B., Chang, B.S., Minn, A.J., et al. (1997). Structure of Bcl-xL-Bak peptide complex: recognition between regulators of apoptosis. Science *275*, 983–986. https://doi.org/10.1126/science.275.5302.983.
5. Zha, H., Aimé-Sempé, C., Sato, T., and Reed, J.C. (1996). Proapoptotic protein Bax heterodimerizes with Bcl-2 and homodimerizes with Bax via a novel domain (BH3) distinct from BH1 and BH2. J. Biol. Chem. *271*, 7440–7444. https://doi.org/10.1074/jbc.271.13.7440.
6. Oltersdorf, T., Elmore, S.W., Shoemaker, A.R., Armstrong, R.C., Augeri, D.J., Belli, B.A., Bruncko, M., Deckwerth, T.L., Dinges, J., Hajduk, P.J., et al. (2005). An inhibitor of Bcl-2 family proteins induces regression of solid tumours. Nature *435*, 677–681. https://doi.org/10.1038/nature03579.
7. Souers, A.J., Leverson, J.D., Boghaert, E.R., Ackler, S.L., Catron, N.D., Chen, J., Dayton, B.D., Ding, H., Enschede, S.H., Fairbrother, W.J., et al. (2013). ABT-199, a potent and selective BCL-2 inhibitor, achieves antitumor activity while sparing platelets. Nat. Med. *19*, 202–208. https://doi.org/10.1038/nm.3048.
8. Barclay, L.A., Wales, T.E., Garner, T.P., Wachter, F., Lee, S., Guerra, R.M., Stewart, M.L., Braun, C.R., Bird, G.H., Gavathiotis, E., et al. (2015). Inhibition of Pro-apoptotic BAX by a noncanonical interaction mechanism. Mol. Cell *57*, 873–886. https://doi.org/10.1016/j.molcel.2015.01.014.
9. Ma, J., Edlich, F., Bermejo, G.A., Norris, K.L., Youle, R.J., and Tjandra, N. (2012). Structural mechanism of Bax inhibition by cytomegalovirus protein vMIA. Proc. Natl. Acad. Sci. USA *109*, 20901–20906. https://doi.org/10.1073/pnas.1217094110.
10. Edlich, F., Banerjee, S., Suzuki, M., Cleland, M.M., Arnoult, D., Wang, C., Neutzner, A., Tjandra, N., and Youle, R.J. (2011). Bcl-x(L) retrotranslocates Bax from the mitochondria into the cytosol. Cell *145*, 104–116. https://doi.org/10.1016/j.cell.2011.02.034.
11. Todt, F., Cakir, Z., Reichenbach, F., Youle, R.J., and Edlich, F. (2013). The C-terminal helix of Bcl-x(L) mediates Bax retrotranslocation from the mitochondria. Cell Death Differ. *20*, 333–342. https://doi.org/10.1038/cdd.2012.131.
12. Petros, A.M., Olejniczak, E.T., and Fesik, S.W. (2004). Structural biology of the Bcl-2 family of proteins. Biochim. Biophys. Acta *1644*, 83–94. https://doi.org/10.1016/j.bbamcr.2003.08.012.
13. Zhang, Y., Tian, L., Huang, G., Ge, X., Kong, F., Wang, P., Xu, Y., and Shi, Y. (2025). Structural basis of BAX pore formation. Science *388*, eadv4314. https://doi.org/10.1126/science.adv4314.
14. Hauseman, Z.J., Harvey, E.P., Newman, C.E., Wales, T.E., Bucci, J.C., Mintseris, J., Schweppe, D.K., David, L., Fan, L., Cohen, D.T., et al. (2020). Homogeneous Oligomers of Pro-apoptotic BAX Reveal Structural Determinants of Mitochondrial Membrane Permeabilization. Mol. Cell *79*, 68–83.e7. https://doi.org/10.1016/j.molcel.2020.05.029.
15. Lee, E.F., Dewson, G., Smith, B.J., Evangelista, M., Pettikiriarachchi, A., Dogovski, C., Perugini, M.A., Colman, P.M., and Fairlie, W.D. (2011). Crystal structure of a BCL-W domain-swapped dimer: implications for the function of BCL-2 family proteins. Structure *19*, 1467–1476. https://doi.org/10.1016/j.str.2011.07.015.
16. O'Neill, J.W., Manion, M.K., Maguire, B., and Hockenbery, D.M. (2006). BCL-XL dimerization by three-dimensional domain swapping. J. Mol. Biol. *356*, 367–381. https://doi.org/10.1016/j.jmb.2005.11.032.
17. Birkinshaw, R.W., Iyer, S., Lio, D., Luo, C.S., Brouwer, J.M., Miller, M.S., Robin, A.Y., Uren, R.T., Dewson, G., Kluck, R.M., et al. (2021). Structure of detergent-activated BAK dimers derived from the inert monomer. Mol. Cell *81*, 2123–2134.e5. https://doi.org/10.1016/j.molcel.2021.03.014.
18. Czabotar, P.E., Westphal, D., Dewson, G., Ma, S., Hockings, C., Fairlie, W.D., Lee, E.F., Yao, S., Robin, A.Y., Smith, B.J., et al. (2013). Bax crystal structures reveal how BH3 domains activate Bax and nucleate its oligomerization to induce apoptosis. Cell *152*, 519–531. https://doi.org/10.1016/j.cell.2012.12.031.
19. Koss, B., Ryan, J., Budhraja, A., Szarama, K., Yang, X., Bathina, M., Cardone, M.H., Nikolovska-Coleska, Z., Letai, A., and Opferman, J.T. (2016). Defining specificity and on-target activity of BH3-mimetics using engineered B-ALL cell lines. Oncotarget *7*, 11500–11511. https://doi.org/10.18632/oncotarget.7204.
20. Jeong, S.Y., Gaume, B., Lee, Y.J., Hsu, Y.T., Ryu, S.W., Yoon, S.H., and Youle, R.J. (2004). Bcl-x(L) sequesters its C-terminal membrane anchor in soluble, cytosolic homodimers. EMBO J. *23*, 2146–2155. https://doi.org/10.1038/sj.emboj.7600225.
21. Wilson-Annan, J., O'Reilly, L.A., Crawford, S.A., Hausmann, G., Beaumont, J.G., Parma, L.P., Chen, L., Lackmann, M., Lithgow, T., Hinds, M.G., et al. (2003). Proapoptotic BH3-only proteins trigger membrane integration of prosurvival Bcl-w and neutralize its activity. J. Cell Biol. *162*, 877–887. https://doi.org/10.1083/jcb.200302144.
22. Mintseris, J., and Gygi, S.P. (2020). High-density chemical cross-linking for modeling protein interactions. Proc. Natl. Acad. Sci. USA *117*, 93–102. https://doi.org/10.1073/pnas.1902931116.
23. Lovell, J.F., Billen, L.P., Bindner, S., Shamas-Din, A., Fradin, C., Leber, B., and Andrews, D.W. (2008). Membrane binding by tBid initiates an ordered series of events culminating in membrane permeabilization by Bax. Cell *135*, 1074–1084. https://doi.org/10.1016/j.cell.2008.11.010.
24. Walensky, L.D., Pitter, K., Morash, J., Oh, K.J., Barbuto, S., Fisher, J., Smith, E., Verdine, G.L., and Korsmeyer, S.J. (2006). A stapled BID BH3 helix directly binds and activates BAX. Mol. Cell *24*, 199–210. https://doi.org/10.1016/j.molcel.2006.08.020.
25. Holmgreen, S.P., Huang, D.C., Adams, J.M., and Cory, S. (1999). Survival activity of Bcl-2 homologs Bcl-w and A1 only partially correlates with their ability to bind pro-apoptotic family members. Cell Death Differ. *6*, 525–532. https://doi.org/10.1038/sj.cdd.4400519.
26. Alimohamadi, H., de Anda, J., Lee, M.W., Schmidt, N.W., Mandal, T., and Wong, G.C.L. (2023). How Cell-Penetrating Peptides Behave Differently from Pore-Forming Peptides: Structure and Stability of Induced Transmembrane Pores. J. Am. Chem. Soc. *145*, 26095–26105. https://doi.org/10.1021/jacs.3c08014.
27. Schmidt, N.W., Mishra, A., Lai, G.H., Davis, M., Sanders, L.K., Tran, D., Garcia, A., Tai, K.P., McCray, P.B., Ouellette, A.J., et al. (2011). Criterion for amino acid composition of defensins and antimicrobial peptides based on geometry of membrane destabilization. J. Am. Chem. Soc. *133*, 6720–6727. https://doi.org/10.1021/ja200079a.
28. Schmidt, N.W., and Wong, G.C.L. (2013). Antimicrobial peptides and induced membrane curvature: geometry, coordination chemistry, and molecular engineering. Curr. Opin. Solid State Mater. Sci. *17*, 151–163. https://doi.org/10.1016/j.cossms.2013.09.004.
29. Lee, M.W., Luo, E.W.C., Silvestre-Roig, C., Srinivasan, Y., Akabori, K., Lemnitzer, P., Schmidt, N.W., Lai, G.H., Santangelo, C.D., Soehnlein, O., et al. (2021). Apolipoprotein Mimetic Peptide Inhibits Neutrophil-Driven

Inflammatory Damage via Membrane Remodeling and Suppression of Cell Lysis. ACS Nano *15*, 15930–15939. https://doi.org/10.1021/acsnano.1c03978.

30. Shearman, G.C., Ces, O., Templer, R.H., and Seddon, J.M. (2006). Inverse lyotropic phases of lipids and membrane curvature. J. Phys. Condens. Matter *18*, S1105–S1124. https://doi.org/10.1088/0953-8984/18/28/S01.
31. Harper, P.E., and Gruner, S.M. (2000). Electron density modeling and reconstruction of infinite periodic minimal surfaces (IPMS) based phases in lipid-water systems. I. Modeling IPMS-based phases. Eur. Phys. J. E *2*, 217–228. https://doi.org/10.1007/PL00013660.
32. Schwarz, U.S., and Gompper, G. (1999). Systematic approach to bicontinuous cubic phases in ternary amphiphilic systems. Phys. Rev. E Stat. Phys. Plasmas Fluids Relat. Interdiscip. Topics *59*, 5528–5541. https://doi.org/10.1103/physreve.59.5528.
33. Tse, C., Shoemaker, A.R., Adickes, J., Anderson, M.G., Chen, J., Jin, S., Johnson, E.F., Marsh, K.C., Mitten, M.J., Nimmer, P., et al. (2008). ABT-263: a potent and orally bioavailable Bcl-2 family inhibitor. Cancer Res. *68*, 3421–3428. https://doi.org/10.1158/0008-5472.CAN-07-5836.
34. Kotschy, A., Szlavik, Z., Murray, J., Davidson, J., Maragno, A.L., Le Toumelin-Braizat, G., Chanrion, M., Kelly, G.L., Gong, J.N., Moujalled, D.M., et al. (2016). The MCL1 inhibitor S63845 is tolerable and effective in diverse cancer models. Nature *538*, 477–482. https://doi.org/10.1038/nature19830.
35. Perez-Riverol, Y., Bai, J., Bandla, C., García-Seisdedos, D., Hewapathirana, S., Kamatchinathan, S., Kundu, D.J., Prakash, A., Frericks-Zipper, A., Eisenacher, M., et al. (2022). The PRIDE database resources in 2022: a hub for mass spectrometry-based proteomics evidences. Nucleic Acids Res. *50*, D543–D552. https://doi.org/10.1093/nar/gkab1038.
36. Gavathiotis, E., Suzuki, M., Davis, M.L., Pitter, K., Bird, G.H., Katz, S.G., Tu, H.C., Kim, H., Cheng, E.H.Y., Tjandra, N., et al. (2008). BAX activation is initiated at a novel interaction site. Nature *455*, 1076–1081. https://doi.org/10.1038/nature07396.
37. Bloch, N.B., Wales, T.E., Prew, M.S., Levy, H.R., Engen, J.R., and Walensky, L.D. (2021). The conformational stability of pro-apoptotic BAX is dictated by discrete residues of the protein core. Nat. Commun. *12*, 4932. https://doi.org/10.1038/s41467-021-25200-7.
38. Some, D., Amartely, H., Tsadok, A., and Lebendiker, M. (2019). Characterization of Proteins by Size-Exclusion Chromatography Coupled to Multi-Angle Light Scattering (SEC-MALS). J. Vis. Exp. *148*. https://doi.org/10.3791/59615.
39. Yang, L., Lazo, E., Byrnes, J., Chodankar, S., Antonelli, S., and Rakitin, M. (2021). Tools for supporting solution scattering during the COVID-19 pandemic. J. Synchrotron Radiat. *28*, 1237–1244. https://doi.org/10.1107/S160057752100521X.
40. Manalastas-Cantos, K., Konarev, P.V., Hajizadeh, N.R., Kikhney, A.G., Petoukhov, M.V., Molodenskiy, D.S., Panjkovich, A., Mertens, H.D.T., Gruzinov, A., Borges, C., et al. (2021). ATSAS 3.0: expanded functionality and new tools for small-angle scattering data analysis. J. Appl. Crystallogr. *54*, 343–355. https://doi.org/10.1107/S1600576720013412.
41. Svergun, D.I. (1992). Determination of the regularization parameter in indirect-transform methods using perceptual criteria. J. Appl. Crystallogr. *25*, 495–503. https://doi.org/10.1107/S0021889892001663.
42. Piiadov, V., Ares de Araújo, E., Oliveira Neto, M., Craievich, A.F., and Polikarpov, I. (2019). SAXSMoW 2.0: Online calculator of the molecular weight of proteins in dilute solution from experimental SAXS data measured on a relative scale. Protein Sci. *28*, 454–463. https://doi.org/10.1002/pro.3528.
43. Rambo, R.P., and Tainer, J.A. (2013). Accurate assessment of mass, models and resolution by small-angle scattering. Nature *496*, 477–481. https://doi.org/10.1038/nature12070.
44. Franke, D., and Svergun, D.I. (2009). DAMMIF, a program for rapid ab-initio shape determination in small-angle scattering. J. Appl. Crystallogr. *42*, 342–346. https://doi.org/10.1107/S0021889809000338.
45. Phillips, J.C., Braun, R., Wang, W., Gumbart, J., Tajkhorshid, E., Villa, E., Chipot, C., Skeel, R.D., Kalé, L., and Schulten, K. (2005). Scalable molecular dynamics with NAMD. J. Comput. Chem. *26*, 1781–1802. https://doi.org/10.1002/jcc.20289.
46. Huang, J., and MacKerell, A.D., Jr. (2013). CHARMM36 all-atom additive protein force field: validation based on comparison to NMR data. J. Comput. Chem. *34*, 2135–2145. https://doi.org/10.1002/jcc.23354.
47. MacKerell, A.D., Bashford, D., Bellott, M., Dunbrack, R.L., Evanseck, J.D., Field, M.J., Fischer, S., Gao, J., Guo, H., Ha, S., et al. (1998). All-atom empirical potential for molecular modeling and dynamics studies of proteins. J. Phys. Chem. B *102*, 3586–3616. https://doi.org/10.1021/jp973084f.
48. Mackerell, A.D., Jr., Feig, M., and Brooks, C.L., 3rd. (2004). Extending the treatment of backbone energetics in protein force fields: limitations of gas-phase quantum mechanics in reproducing protein conformational distributions in molecular dynamics simulations. J. Comput. Chem. *25*, 1400–1415. https://doi.org/10.1002/jcc.20065.
49. Durell, S.R., Brooks, B.R., and Ben-Naim, A. (1994). Solvent-Induced Forces between Two Hydrophilic Groups. J. Phys. Chem. *98*, 2198–2202. https://doi.org/10.1021/j100059a038.
50. Jorgensen, W.L., Chandrasekhar, J., Madura, J.D., Impey, R.W., and Klein, M.L. (1983). Comparison of simple potential functions for simulating liquid water. J. Chem. Phys. *79*, 926–935. https://doi.org/10.1063/1.445869.
51. Neria, E., Fischer, S., and Karplus, M. (1996). Simulation of activation free energies in molecular systems. J. Chem. Phys. *105*, 1902–1921. https://doi.org/10.1063/1.472061.
52. Beglov, D., and Roux, B. (1994). Finite representation of an infinite bulk system: Solvent boundary potential for computer simulations. J. Chem. Phys. *100*, 9050–9063. https://doi.org/10.1063/1.466711.
53. Luo, Y., and Roux, B. (2010). Simulation of Osmotic Pressure in Concentrated Aqueous Salt Solutions. J. Phys. Chem. Lett. *1*, 183–189. https://doi.org/10.1021/jz900079w.
54. Miyamoto, S., and Kollman, P.A. (1992). Settle: An analytical version of the SHAKE and RATTLE algorithm for rigid water models. J. Comp. Chem. *13*, 952–962. https://doi.org/10.1002/jcc.540130805.
55. Ryckaert, J.-P., Ciccotti, G., and Berendsen, H.J.C. (1977). Numerical integration of the cartesian equations of motion of a system with constraints: molecular dynamics of n-alkanes. J. Comp. Phys. *23*, 327–341. https://doi.org/10.1016/0021-9991(77)90098-5.
56. Ma, Q., Izaguirre, J.A., and Skeel, R.D. (2003). Verlet-I/R-RESPA/Impulse is Limited by Nonlinear Instabilities. SIAM J. Sci. Comput. *24*, 1951–1973. https://doi.org/10.1137/S1064827501399833.
57. Bussi, G., Donadio, D., and Parrinello, M. (2007). Canonical sampling through velocity rescaling. J. Chem. Phys. *126*, 014101. https://doi.org/10.1063/1.2408420.
58. Feller, S.E., Zhang, Y., Pastor, R.W., and Brooks, B.R. (1995). Constant pressure molecular dynamics simulation: The Langevin piston method. J. Chem. Phys. *103*, 4613–4621. https://doi.org/10.1063/1.470648.
59. Tuckerman, M., Berne, B.J., and Martyna, G.J. (1992). Reversible multiple time scale molecular dynamics. J. Chem. Phys. *97*, 1990–2001. https://doi.org/10.1063/1.463137.
60. Darden, T., York, D., and Pedersen, L. (1993). Particle mesh Ewald: An N·log(N) method for Ewald sums in large systems. J. Chem. Phys. *98*, 10089–10092. https://doi.org/10.1063/1.464397.
61. Essmann, U., Perera, L., Berkowitz, M.L., Darden, T., Lee, H., and Pedersen, L.G. (1995). A smooth particle mesh Ewald method. J. Chem. Phys. *103*, 8577–8593. https://doi.org/10.1063/1.470117.
62. Skeel, R.D. (2016). An alternative construction of the Ewald sum. Mol. Phys. *114*, 3166–3170. https://doi.org/10.1080/00268976.2016.1222455.

63. Humphrey, W., Dalke, A., and Schulten, K. (1996). VMD: visual molecular dynamics. J. Mol. Graph. *14*, 33–38. https://doi.org/10.1016/0263-7855(96)00018-5.

64. Harris, C.R., Millman, K.J., van der Walt, S.J., Gommers, R., Virtanen, P., Cournapeau, D., Wieser, E., Taylor, J., Berg, S., Smith, N.J., et al. (2020). Array programming with NumPy. Nature *585*, 357–362. https://doi.org/10.1038/s41586-020-2649-2.

65. Hunter, J.D. (2007). Matplotlib: A 2D Graphics Environment. Comput. Sci. Eng. *9*, 90–95. https://doi.org/10.1109/MCSE.2007.55.

66. Bird, G.H., Bernal, F., Pitter, K., and Walensky, L.D. (2008). Synthesis and biophysical characterization of stabilized alpha-helices of BCL-2 domains. Methods Enzymol. *446*, 369–386. https://doi.org/10.1016/S0076-6879(08)01622-4.

67. Pitter, K., Bernal, F., Labelle, J., and Walensky, L.D. (2008). Dissection of the BCL-2 family signaling network with stabilized alpha-helices of BCL-2 domains. Methods Enzymol. *446*, 387–408. https://doi.org/10.1016/S0076-6879(08)01623-6.

68. Wales, T.E., and Engen, J.R. (2006). Hydrogen exchange mass spectrometry for the analysis of protein dynamics. Mass Spectrom. Rev. *25*, 158–170. https://doi.org/10.1002/mas.20064.

69. Kuwana, T., Mackey, M.R., Perkins, G., Ellisman, M.H., Latterich, M., Schneiter, R., Green, D.R., and Newmeyer, D.D. (2002). Bid, Bax, and lipids cooperate to form supramolecular openings in the outer mitochondrial membrane. Cell *111*, 331–342. https://doi.org/10.1016/s0092-8674(02)01036-x.

70. Elias, J.E., and Gygi, S.P. (2007). Target-decoy search strategy for increased confidence in large-scale protein identifications by mass spectrometry. Nat. Methods *4*, 207–214. https://doi.org/10.1038/nmeth1019.

71. Schilling, B., Rardin, M.J., MacLean, B.X., Zawadzka, A.M., Frewen, B.E., Cusack, M.P., Sorensen, D.J., Bereman, M.S., Jing, E., Wu, C.C., et al. (2012). Platform-independent and label-free quantitation of proteomic data using MS1 extracted ion chromatograms in skyline: application to protein acetylation and phosphorylation. Mol. Cell. Proteomics *11*, 202–214. https://doi.org/10.1074/mcp.M112.017707.

STAR★METHODS

KEY RESOURCES TABLE

REAGENT or RESOURCE	SOURCE	IDENTIFIER
Antibodies		
Mouse monoclonal anti-BCL-X_L H-5	Santa Cruz	Cat# sc-8392; RRID: AB_626739
Mouse monoclonal anti-FLAG M2	Sigma-Aldrich	Cat# A8592; RRID: AB_439702
Mouse monclonal anti-V5	Thermo Fisher Scientific	Cat# R961-25; RRID: AB_2556565
Mouse monoclonal anti-VDAC1 B-6	Santa Cruz	Cat# sc-390996; RRID: AB_2750920
Mouse monoclonal anti-BAX 2D2	Santa Cruz	Cat# sc-20067; RRID: AB_626726
Mouse monocloncal anti-BAX B9	Santra Cruz	Cat# sc-7480; RRID: AB_626729
Rabbit monoclonal anti-BCL-w 31H4	Cell Signaling Technology	Cat# 2724S; RRID: AB_10691557
Bacterial and Virus Strains		
One Shot BL21(DE3) Competent Cells	Invitrogen	Cat# C600003;
Chemicals, Peptides, and Recombinant Proteins		
Complete Protease Inhibitor Tablet Cocktail	Sigma-Aldrich	Cat# 16829800
SimplyBlue SafeStain	Thermo Fisher Scientific	Cat# LC6065
SeeBlue Plus2 Pre-Stained Protein Standard	Invitrogen	Cat# LC5925
IPTG	Gold Biotechnology	Cat# I2481C
Chitin bead resin	New England Biolabs	Cat# S6651S
Ni-NTA agarose	Qiagen	Cat# 30210
Sepharose CL-2B	GE Healthcare Life Sciences	Cat# 17014001
Dithiothreitol (DTT)	Gold Biotechnology	Cat# DTT25
1,2-dioleoyl-sn-glycero-3-phosphoethanolamine (DOPE)	Avanti	Cat# 850725P
2-dioleoyl-sn-glycero-3-phosphocholine (DOPC)	Avanti	Cat# 850375P
1-palmitoyl-2-oleoyl-sn-glycero-3-phosphocholine	Avanti	Cat# 850457C
1-palmitoyl-2-oleoyl-sn-glycero-3-phosphoethanolamine	Avanti	Cat# 850757C
L-α-phosphatidylinositol (Liver, Bovine) (sodium salt)	Avanti	Cat# 840042C
1,2-dioleoyl-sn-glycero-3-phospho-L-serine (sodium salt)	Avanti	Cat# 840035C
Cardiolipin (Heart, Bovine) (sodium salt)	Avanti	Cat# 840012C
n-Dodecylphosphocholine (Fos-12)	Anatrace	Cat# F308
n-Tridecylphosphocholine (Fos-13)	Anatrace	Cat# F310
n-Tetradecylphosphocholine (Fos-14)	Anatrace	Cat# F312
N,N-Dimethyl-n-dodecylamine N-oxide (LDAO)	Cube Biotechnology	Cat# 16006
AffiPro Nep-2 column	AffiPro	Cat# AP-PC-004
Thrombin	Sigma	Cat# GE27-0846-01
Trypsin	Promega	Cat# VA 9000
Fluorescein 5-malemide	AAT Bioquest	Cat# 130
Glu-fibrinopeptide	Sigma	Cat# F3261
Bis(sulfosuccinimidyl) glutarate (BS2G)	ThermoFischer Scientific	Cat# 21610
Sulfo-NHS (N-hydroxysulfosuccinimide)	Sigma	Cat# 56485
1-ethyl-3-(3-dimethylaminopropyl) carbodiimide hydrochloride (EDC)	Sigma	Cat# 03450
Ethylenediamine (EDA)	Sigma	Cat# N1925
2,2′-(ethylenedioxy)bis(ethylamine) (EDDA)	Sigma	Cat# 385506
Empore C18 SPE Extraction Disks	3M	Cat# 98060402173
Accucore C18 resin	ThermoFischer Scientific	Cat# 03-898-110

(*Continued on next page*)

Continued

REAGENT or RESOURCE	SOURCE	IDENTIFIER
DMEM	Gibco	Cat# 11960044
Fetal Bovine Serum (FBS)	GeminiBio	SKU# 100-106
Penicillin-Streptomycin	Gibco	Cat#15140122
L-Glutamine	Gibco	Cat# 25030081
10X RIPA lysis buffer	Millipore	Cat# 20-188
Anti-FLAG M2 Magnetic Beads	Sigma-Aldrich	Cat# M8823
Anti-V5 D3H8Q Magnetic Beads	Cell Signaling Technology	Cat# 31628
Tween 20	Sigma-Aldrich	Cat# P1379
4X LDS Sample Buffer	Thermo Fisher Scientific	Cat# NP0008
ethylene glycol-bis(β-aminoethyl ether)-N,N,N',N'-tetraacetic acid (EGTA)	Sigma-Aldrich	Cat# 324626
Sucrose	Sigma-Aldrich	Cat# S0389
CHAPS	Sigma-Aldrich	Cat# 220201
PEG-it Virus Precipitation Solution	System Bio	Cat# LV810A-1
Recombinant BAX WT	Walensky Lab	N/A
Recombinant BAXΔN (aa 52-192)	Walensky Lab	N/A
Recombinant BAX D2C	Walensky Lab	N/A
Recombinant BAX α2-α5 (aa 53-128, C62S, C126S)	Walensky Lab	N/A
Recombinant BCL-w WT	Walensky Lab	N/A
Recombinant BCL-wΔC (aa 1-156)	Walensky Lab	N/A
Recombinant BCL-wΔN (aa 40-193)	Walensky Lab	N/A
Recombinant BCL-X_L WT	Walensky Lab	N/A
Recombinant BCL-wΔNΔC (aa 40-156)	Walensky Lab	N/A
Recombinant BCL-w G94E	Walensky Lab	N/A
Recombinant BCL-w E109A/E114A/E116A/E124A	Walensky Lab	N/A
Recombinant BCL-w α2-α5 (aa 42-112, C107S)	Walensky Lab	N/A
Recombinant BCL-w α1-α5 (aa 1-112)	Walensky Lab	N/A
Recombinant BCL-w α1-α6 (aa 1-132)	Walensky Lab	N/A
Recombinant BCL-w α1-α8 (aa 1-156)	Walensky Lab	N/A
Critical Commercial Assays		
Q5 Site Directed Mutagenesis Kit	New England Biolabs	Cat# E0554S
Pierce BCA Protein Assay Kit	ThermoFisher Scientific	Cat# 23225
Rat/Mouse Cytochrome c Quantikine ELISA Kit	R&D Systems	Cat# MCTC0
CellEvent™ Caspase-3/7	Thermo Fisher Scientific	Cat# C10430
Lipofectamine LTX Reagent with Plus Reagent	Thermo Fisher Scientific	Cat# 15338100
Pierce Silver Stain Kit	ThermoFisher Scientific	Cat# 24612
Deposited Data		
HDX MS Datasets	Wales/Walensky Labs	PRIDE ID: PXD049315
Experimental Models: Cell Lines		
Human Embryonic Kidney 293T	ATCC	CRL-3216
Mouse Embryonic Fibroblasts (MEFs)	ATCC	CRL-2991
Bcl-w$^{-/-}$ MEFs	Walensky Lab	N/A
Bcl-w$^{-/-}$ MEFs reconstituted with WT, G94E, E4A, or G94E/E4A BCL-w protein	Walensky Lab	N/A
p185+*Arf*$^{-/-}$*Mcl-1*^{del}*Bcl-w*^{recon} B-ALL	Opferman Lab	N/A
Recombinant DNA		
Plasmid PTYB1	New England Biolabs	Cat# E6901
Plasmid pET28a	Sigma	Cat# 69864

(*Continued on next page*)

Continued

REAGENT or RESOURCE	SOURCE	IDENTIFIER
Plasmid PTYB1_BAX_WT	Walensky Lab	N/A
Plasmid PTYB1_BAX_ΔN (aa 52-192)	Walensky Lab	N/A
Plasmid PTYB1_BAX_D2C	Walensky Lab	N/A
Plasmid PTYB1_BCL-w_WT	Walensky Lab	N/A
Plasmid PTYB1_BCL-w_ΔC (aa 1-156)	Walensky Lab	N/A
Plasmid PTYB1_BCL-w_ΔN_thrombin	Walensky Lab	N/A
Plasmid PTYB1_BCL-X_L_WT	Walensky Lab	N/A
Plasmid PTYB1_BCL-w_ΔN_ΔC_thrombin (aa1-156)	Walensky Lab	N/A
Plasmid PTYB1_BCL-w_G94E	Walensky Lab	N/A
Plasmid PTYB1_BCL-w_E109A_E114A_E116A_E124A	Walensky Lab	N/A
Plasmid pET28a_BCL-w α2-α5 (aa 42-112, C107S)	Walensky Lab	N/A
Plasmid pET28a_BCL-w_ α1-α5 (aa 1-112)	Walensky Lab	N/A
Plasmid pET28a_BCL-w_α1-α6 (aa 1-132)	Walensky Lab	N/A
Plasmid pET28a_BCL-w_α1-α8 (aa 1-156)	Walensky Lab	N/A
Plasmid pMIG_BCL-w	Walensky Lab	N/A
Plasmid pMIG_BCL-w_E109A_E114A_E116A_E124A	Walensky Lab	N/A
Plasmid pMIG_BCL-w_G94E	Walensky Lab	N/A
Plasmid pMIG_BCL-w_G94E_E109A_ E114A_E116A_E124A	Walensky Lab	N/A
Plasmid pCMV6_BCL-w_V5	Walensky Lab	N/A
Plasmid pCMV6_BCL-w_FLAG	Walensky Lab	N/A
Software and Algorithms		
GraphPad Prism	Graphpad Software Inc.	https://www.graphpad.com; RRID: SCR_002798
The PyMol Molecular Graphics System, Version 2.1.1	Schrodinger, LLC	http://www.pymol.org; RRID: SCR_000305
Matlab	Math Works	https://www.mathworks.com/products/matlab.html
ProteinLynx Global Server (PLGS) 3.0.1	Waters Corporation	http://www.waters.com/waters/en_US/ProteinLynx-Global-SERVER-(PLGS)/nav.htm?cid=513821&locale=en_US; RRID: SCR_016664
DynamX 3.0	Waters Corporation	https://www.waters.com/nextgen/us/en/library/library-details.html?documentid=720005145&t=waters-DynamXHDX DataAnalysisSoftware-720005145
GNOM	Svergun[41]	https://www.embl-hamburg.de/biosaxs/gnom.html
DAMMIF	Franke and Svergun[44]	https://www.embl-hamburg.de/biosaxs/dammif.html
DAMAVER	Franke and Svergun[44]	https://www.embl-hamburg.de/biosaxs/damaver.html
DAMFILT	Franke and Svergun[44]	DAMAVER manual - Biological small angle scattering - EMBL Hamburg
ATSAS (3.0.3) software	Manalastas-Cantos[40]	https://www.embl-hamburg.de/biosaxs/download.html
Skyline v20	Schilling et al.[71]	https://skyline.ms/project/home/software/Skyline/begin.view
ASTRA 8 software	Technical Note TN1006, Wyatt Technology, 2024	https://www.wyatt.com/blogs/discover-tricks-and-tips-with-our-technical-notes.html

(*Continued on next page*)

Continued

REAGENT or RESOURCE	SOURCE	IDENTIFIER
Other		
Superdex 75 10/300 GL size exclusion column	Cytiva	Cat# 29148721
Superose 6 Increase 10/300 GL size exclusion column	Cytiva	Cat# 29091596
Superdex 200 Increase 10/300 GL size exclusion column	Cytiva	Cat# 28990944
Superdex 200 increase 5/150 GL size exclusion column	Cytiva	Cat# 28990945
PD-10 desalting column with Sephadex G-25 resin	Cytiva	Cat# 17085101

EXPERIMENTAL MODEL AND SUBJECT DETAILS

Mouse Liver Mitochondria

Liver mitochondria were isolated, as described below, from AlbCre^{pos}*Bax*$^{f/f}$*Bak*$^{-/-}$ mice.[24]

METHOD DETAILS

Recombinant Protein Expression and Purification

Full length (FL) BAX (aa 1-192), FL BCL-w (aa 1- 193), and FL BCL-X_L (aa 1-233) were cloned into pTYB1 as previously described.[14,36] BCL-w and BAX mutations, including BCL-wΔN and BAXΔN (generated by installing a thrombin cleavage site LVPRGSPGG after amino acid [aa] 39 of FL BCL-w and after aa 51 of FL BAX), BCL-w ΔC (aa 1-156), BCL-w ΔNΔC (aa 40-156) (generated by installing the same thrombin cleavage site as above after aa 39 of BCL-w ΔC) and BAX D2C (D2C, C62S, C126S) were generated through PCR based site-directed mutagenesis (Q5 Site Directed Mutagenesis Kit, New England BioLabs) and confirmed by DNA sequencing. BCL-w G94E and BCL-w E4A (E109A/E114A/E116A/E124A) were generated from the FL WT pTYB1 vector via site-directed mutagenesis (Azenta Life Sciences) and confirmed by DNA sequencing. BAX, BCL-w, and BCL-X_L constructs were expressed in *Escherichia coli* BL21(DE3). BAX protein expression was induced with 1 mM isopropyl β-D-1-thiogalactopyranoside (IPTG) for 4 hours at 30°C, whereas BCL-w proteins were induced with 1 mM IPTG overnight at 16°C and BCL-X_L proteins were induced with 0.5 mM IPTG overnight at 16°C. Bacterial pellets were resuspended in lysis buffer (20 mM Tris pH 7.2, 250 mM NaCl) containing complete protease inhibitor tablets (Roche) and microfluidized (M-110L, Microfluidics), followed by centrifugation at 20,000 rpm for 45 min. BAX, BCL-w, and BCL-X_L proteins were purified from clarified lysate by chitin affinity chromatography using chitin resin (NEB) equilibrated in lysis buffer by gravity flow. Following 3 washes with lysis buffer, BAX, BCL-w, and BCL-X_L constructs were cleaved from the chitin beads by overnight incubation with lysis buffer containing 10 mg/mL dithiothreitol (DTT) at 4°C. Protein-containing eluate was concentrated (10 kDa spin concentrator, Millipore) and purified by size exclusion chromatography (SEC) on a Superdex 75 increase 10/300 GL (Cytiva) in FPLC buffer (20 mM HEPES, pH 7.2, 150 mM KCl). FL BCL-w and FL BAX bearing a thrombin cleavage site for BCL-wΔN and BAXΔN preparation was treated with thrombin (Sigma) overnight at 4°C and then repurified by SEC as above. The degree of thrombin cleavage was assessed by SDS-PAGE electrophoresis and Coomassie staining. Protein purity and identity for each construct was confirmed by western blot analysis using 2D2 mouse monoclonal antibody (Santa Cruz Biotechnology Cat# sc-20067; RRID: AB_626726) for BAX, 31H4 rabbit monoclonal antibody (Cell Signaling Technology Cat# 2724S; RRID:AB 10691557) for BCL-w, and H-5 mouse monoclonal antibody (Santa Cruz Biotechnology Cat# sc-8392; RRID: AB_626739) for BCL-X_L.

BAX α2-α5 (aa 53-128, C62S, C126S) and BCL-w α2-α5 (aa 42-112, C107S), each containing an N-terminal His_6-GFP tag were cloned into the pET28a vector, as previously described.[37] BCL-w α1-α5 (aa 1-112), BCL-w α1-α6 (aa 1-132), and BCL-w α1-α8 (aa 1-156) were generated using restriction enzyme cloning by Azenta Life Sciences through insertion of NdeI and XhoI cut sites flanking the indicated truncation, followed by restriction enzyme cloning into the pET28a vector with an N-terminal His_6-GFP tag. The BAX and BCL-w truncated constructs were expressed in *E.coli* BL21(DE3) with 0.5 mM IPTG induction overnight at 16°C. Bacterial pellets were resuspended in TBS (20 mM Tris pH 8.0, 150 mM NaCl) containing protease inhibitor tablets (Roche) and lysed by a microfluidizer (M-110L, Microfluidics). Lysates were then clarified by centrifugation at 20,000 rpm for 45 min at 4°C. Purification was achieved by Ni-NTA (Qiagen) gravity flow chromatography, with the resin pre-equilibrated in TBS. After a 20 mL TBS wash, proteins were eluted from the column by sequential washes with 12.5 mL TBS containing 5 mM, 40 mM, 70 mM, 100 mM, 200 mM, and 300 mM imidazole. Protein purity was assessed by SDS-PAGE electrophoresis and Coomassie staining. Fractions containing BAX or BCL-w constructs were combined, concentrated, and purified by SEC on a Superdex 200 increase 10/300 GL column (Cytiva). The isolated proteins were reinjected for size analysis by SEC using a Superdex 200 column.

Preparation of BAX Oligomers and BCL-w Dimers

To induce BAX oligomerization, monomeric BAX protein (20 μM) was combined with 3 mM n-dodecylphosphocholine (Fos-12) and incubated overnight at 4°C. The protein-detergent sample was then concentrated using a 30 kDa spin concentrator (Millipore) and

purified by SEC on a Superose 6 increase 10/300 GL column (Cytiva) in detergent-free FPLC buffer (20 mM HEPES, pH 7.2, 150 mM KCl). To induce BCL-w and BCL-X_L dimerization, monomeric protein (20 μM) was incubated with 3 mM of the indicated detergents overnight at 4°C. GFP-BCL-w truncates were treated with 1 mM Fos-14 and incubated overnight at 4°C. The protein-detergent sample was then concentrated with a 30 kDa spin concentrator (Millipore) and purified by SEC in detergent-free FPLC buffer (20 mM HEPES, pH 7.2, 150 mM KCl) using a Superose 6 increase 10/300 GL column (Cytiva) or Superdex 200 increase 10/300 GL column (Cytiva). For the comparative assessment of BAX_O and BCL-w_D SEC elution profiles, n-dodecylphosphocholine (Fos-12) was applied given its prior use in characterizing pro-apoptotic BAX_O.[14] For the detergent screen, phoscholines (Fos-12, Fos-13, Fos-14) or n,n-dimethyl-n-dodecylamine-n-oxide (LDAO) at 3 μM were incubated with 5 mL of 20 μM FL BCL-w. Subsequent biochemical studies were performed using Fos-14, except for Small Angle X-ray Scattering (SAXS) studies, which was optimally compatible with LDAO.

Analysis of BAX and BCL-w Proteins by Size Exclusion Chromatography

The BAX D2C monomer, generated and purified as described above, was incubated with 20-fold excess of the cysteine-reactive dye fluorescein-5-malemide (ThermoFisher) for 2 hours at room temperature. Excess dye was then removed by a PD-10 desalting column using Sephadex G-25 resin according to the manufacturer's protocol (Cytiva). The FITC-labeled BAX monomer was then subjected to detergent-induced oligomerization, as described above. FITC-BAX_O (10 μM) and either BCL-w_M or BCL-w_D were incubated at the indicated ratio (calculated by monomer) at room temperature for 1 hour. Samples were then analyzed by SEC on a Superose 6 increase 10/300 GL column, monitoring wavelengths 280, 488, and 647 nm. The BAX_O-only control contained the same amount of BAX_O as the BCL-w treated conditions and was similarly reinjected on the Superose 6 column for SEC analysis.

Multi-Angle Light Scattering

BCL-w_D was subjected to an additional SEC purification by a Superdex 200 increase 10/300 GL column in detergent-free FPLC buffer (20 mM HEPES, pH 7.2, 150 mM KCl) and analyzed directly by an inline miniDAWN Multi-Angle Light Scatterer (MALS) with an Optilab Refractive Index (RI) System (Wyatt Technology).[38] Samples were run at 0.4 mL/min using an Arc Premier HPLC with a UV detector (Waters Inc., USA). MALS measurements were taken using a 658 nm laser with 3 multi-angle detectors at 4 °C and paired with UV (A_{280}) and RI measurements. BCL-w_D molar mass was determined by protein conjugate analysis using ASTRA 8 software (Wyatt Technology).

Assessment of BCL-w Dimerization in Cells

Cell lines expressing FLAG-tagged and V5-tagged BCL-w were generated by transient transfection using Lipofectamine LTX reagent, in accordance with the manufacturer's protocol (ThermoFisher). Briefly, 500 ng of plasmid DNA was transfected into $5x10^5$ low-passage HEK 293T cells (ATCC) seeded in 6-well plates and cultured in DMEM (Gibco), supplemented with 10% (v/v) FBS, 100 μg/mL streptomycin (Gibco) and 100 U/mL penicillin (Gibco). Following transfection at 70–80% confluency, cells were allowed to grow for 48 hours. Cell pellets from transfected cell populations were lysed in 1X RIPA buffer prepared from 10X RIPA Buffer (Sigma Aldrich) supplemented with a protease inhibitor tablet, followed by centrifugation and filtration to remove debris. Clarified lysates were quantified by the Bradford assay (Pierce) and 1 mg of the lysate was subjected to immunoprecipitation by incubation with immobilized and pre-washed mouse monoclonal anti-FLAG M2 magnetic beads (Sigma-Aldrich) or rabbit monoclonal anti-V5 magnetic beads (Cell Signaling Technology) at 4 °C overnight, followed by removal of the supernatant and washing the beads with lysis buffer (x3), PBS supplemented with 0.1% Tween-20 (x2) and PBS pH 7.2 (x2). Bead-bound proteins were eluted by boiling in 1x LDS loading buffer containing 100 mM DTT for 10 min and then subjected to gel electrophoresis. Proteins were transferred onto nitrocellulose membranes using the iBlot 7-Minute Blotting System, blocked in 5% milk in PBS-Tween (PBST), and incubated at 1:1000 with the corresponding primary antibody (FLAG: Sigma-Aldrich Cat# A8592, RRID:AB_439702; V5: Thermo Fisher Scientific Cat# R961-25, RRID:AB_2556565) in 3% BSA in PBST. Western blots were developed using the ECL Prime Western Blotting Detection Reagent (Amersham).

Small Angle X-ray Scattering Analysis of Dimeric BCL-w

SEC-SAXS was performed at the 16ID-LiX Beamline (National Synchrotron Light Source II, Brookhaven National Laboratory). BCL-w_D (6 mg/mL, 100 μL) was injected into the Superdex 200 Increase 5/150 GL column (Cytiva) connected to a Shimadzu bio-inert HPLC system. The sample flowed through the column at a rate of 0.35 mL/min and was directed to the flow cell for simultaneous SAXS and WAXS measurements. The X-ray wavelength was 0.8203 Å and two setups (small- and wide-angle X-ray scattering) were used simultaneously to cover scattering q ranges of $0.005 < q < 3.19$ Å^{-1}, where $q = (4\pi/\lambda)\sin\theta$, with 2θ representing the scattering angle and λ indicating the X-ray wavelength. A total of 750 frames were collected with an exposure time of 2 sec. The running buffer consisted of 250 mM KCl, pH 7.2, 5% glycerol, 1 mM DTT, and 0.5 mM LDAO. The data were processed using NSLSII Jupyter notebook. Subsequent buffer subtraction, peak selection, and profile analysis were performed using Lixtools[39] and ATSAS (3.0.3) software.[40] The radius of gyration (Rg) was determined by generating a Guinier plot in the range of $qRg < 1.3$. For comparison, Rg was also calculated in real and reciprocal spaces using program GNOM in q range up to 0.30 Å^{-1}.[41] The pair-distance distribution function *P*(r) and maximum dimension (Dmax) were also calculated using GNOM. Molecular weights were estimated using methods based on corrected Porod volume[42] and correlation volume[43] within the q range of $0 < q < 0.3$ Å-1. Thirty-two ab-initio shape

Please cite this article in press as: Newman et al., Inhibition of oligomeric BAX by an anti-apoptotic dimer, Cell (2025), https://doi.org/10.1016/j.cell.2025.10.037

reconstructions (molecular envelopes) were generated independently using DAMMIF in slow mode, averaged with DAMAVER, and then filtered with DAMFILT to generate the final model.[44]

Molecular Dynamics Simulation

We performed both simulations and optimizations using SAXS-based restraints, which were introduced using a restraining potential,

$$U(r_i, t_n) = \frac{1}{2}\alpha(\|\boldsymbol{r}_i(t_n)\| - R)^2\theta(\|\boldsymbol{r}_i(t_n)\| - R),$$

where α is a real constant and $\boldsymbol{r}_i(t_n) = \boldsymbol{x}_i(t_n) - \boldsymbol{X}_{i,n}$ is a vector pointing toward C_α of the i-th residue $\boldsymbol{x}_i(t_n)$ from the centroid of the nearest SAXS bead $\boldsymbol{X}_i$. Atomic coordinates are parameterized by the time $t_n = n{\cdot}\delta t$ at step n of our simulation (the timestep δt = 1 during optimizations). A Heaviside step function $\theta(x)$ ensures that the potential is zero below a threshold radius R for the restraint. This results in a restoring force on the associated C_α atom,

$$\boldsymbol{F}_i(t_n) = -\alpha(\|\boldsymbol{r}_i(t_n)\| - R_i)\frac{\boldsymbol{r}_i(t_n)}{|\boldsymbol{r}_i(t_n)|},$$

that is directed radially inward toward the centroid. The SAXS beads are specified by fitting the SAXS experimental data and their coordinates remain fixed during the simulation. The bead closest to the i-th alpha carbon is continuously updated, giving the coordinate $\boldsymbol{X}_{i,n}$ its step dependence. This ultimately forces the protein to lie within a convex hull formed by balls of radius R about the bead centroids. The probability for violations for coordinate set $\{\boldsymbol{r}_i\}$ follow a Gaussian profile given by the respective Boltzmann factors

$$P(\{\boldsymbol{r}_i\}) \propto exp\left[-\frac{\alpha}{2k_BT}\sum_{i=1}^{N}\left|\boldsymbol{r}_i - R\right|^2\right].$$

A multi-stage optimization approach was used to model BCL-w dimers and maintain consistency with the bead-based SAXS profiles. We began by extracting a crystallographic BCL-w dimer[15] (PDB ID 2Y6W) and aligning it to the principle axes and center-of-mass of the bead profile. Next, we reverted non-native mutations in this structure to wild-type and reconstructed the missing N- and C-terminal residues using a loop modeling procedure. Our SAXS constraint strategy was used for all modeling and optimization steps (a = 1). The N-termini of the BCL-w dimer were modeled entirely from first principles. We partially templated the C-terminus by introducing an ideal α9 helix and orienting it to minimize clash with the protein atoms and shell constraints (aa 157-173, EEARRLREGNWASVRTV). Loop regions were then constructed from a library of spatial restraints and refined using an optimization procedure (residues 1-7, 148-160, 174-193) while keeping other atoms fixed. A second stage of loop refinement was then performed by subjecting the full termini to a simulated annealing protocol. These calculations were facilitated by the MODELLER library [MOD1, MOD2]. Refinement of the full complex was achieved using 250 ps implicit-solvent MD simulations with the SAXS-defined restraint potential. Identical calculations were then performed using 5 ns explicit solvent simulations and this ensemble was used for analysis. Optimizations were performed at several characteristic radii (R = 8 Å, R = 10 Å, and R = 12 Å) and consistency assessed using difference maps.

Molecular dynamics simulations were driven by the NAMD 2.14 code[45] and the CHARMM36 protein[45–48] force field. Implicit solvent calculations utilized the Generalized Born Implicit Solvent model with a hydrophobic contribution proportional to the protein's solvent accessible surface area (surface tension = 5.0 x 10^{-3} kcal mol^{-1} $Å^{-2}$). Each implicit solvent simulation began with 2000 steps of CG minimization followed by an initial 50 ps run with a harmonic restraint (k_{prot} = 5.0 kcal mol^{-1} $Å^{-2}$) that localized alpha carbons near their initial positions. This was followed by 250 ps of production simulation without the initial restraint. Irrespective of the stage, a SAXS-based restraint was used with all implicit solvent simulations. Explicit solvent simulations utilized TIP3P water[49–51] (with a 25 Å padding layer) and were supplemented with 0.15 M K^+/Cl^- to ensure electrical neutrality.[52,53] We employed rigid bond constraints[54,55] to achieve numerical stability at a timestep of δt = 2 fs.[56] Our NVT calculations applied a Langevin thermostat to heavy atoms for temperature control (T = 300.0 K; damping γ = 1.0 ps^{-1}),[57] while NPT simulations controlled pressure with a Langevin piston (target P = 101.325 kPa; period = 100.0 fs; decay time = 50.0 fs).[58] Anisotropic cell fluctuations were allowed and multiple time-stepping was used for nonbonded interactions,[59] with short-range interactions evaluated every 2 fs and full electrostatics every 4 fs. Short-range interactions were cut off at 1.2 nm and smoothed with sigmoidal rescaling for atoms separated by more than 1.0 nm. Smoothed particle mesh Ewald (PME) was used for long-range electrostatics.[60–62] Equilibration began with a 2000 step conjugate gradient (CG) minimization followed by 1.0 ns of NVT equilibration with all protein atoms fixed. Next, a harmonic constraint potential (k_{prot} = 5 kcal mol^{-1} $Å^{-2}$) was applied to hold alpha carbons near their initial positions while 2000 steps of CG minimization and 2.0 ns of NPT equilibration were used to relax the protein. All constraints were then removed and production calculations were executed in NPT ensemble for indicated durations. Trajectory samples were captured every 5 ps. Analysis was facilitated, in part, by VMD[63] and the MDAnalysis library [MDA1, MDA2].

To support our MD analyses, we defined distance maps $\boldsymbol{D}_{ij} = \langle\|\boldsymbol{x}_i(s) - \boldsymbol{x}_j(s)\|\rangle$ between atoms in a simulation trajectory or structural ensemble. In this equation, $\boldsymbol{x}_i, \boldsymbol{x}_j$ are the coordinates of the alpha carbons from residues i,j, angular brackets denote averaging over all members of the ensemble $\langle f\rangle = N^{-1}\Sigma_{n=1}^{N} f(s_n)$, and $\|\cdot\|$ is the Euclidean norm. We further quantified relative shifts in

structure using the distance difference map (DDM) $\Delta_{ij}^{AB} = \boldsymbol{D}_{ij}^{A} - \boldsymbol{D}_{ij}^{B}$, between distance maps $\boldsymbol{D}^{A}, \boldsymbol{D}^{B}$ that correspond to distinct ensembles *A* and *B*, respectively. Entries of Δ^{AB} with a positive sign indicate that a pair of residues are further apart in structure *Ai*, while a negative sign indicates the converse. All maps were calculated using Python-based analysis tools, where the NumPy[64] library performs the numerical analysis and Matplotlib[65] is used for data visualization.

Peptide Synthesis

Stapled peptides (SAH-BCL-$w_{\alpha1}$, aa 9-25: DTRALVADFVGYXLRQX; SAH-$BAX_{\alpha1}$, aa 15-35: SSEQIBKTGALLLQGXIQDXA; X = S-pentenyl alanine; B = norleucine) were synthesized, derivatized with either biotin or acetyl at the N-terminus, purified, and quantified by amino acid analysis as reported in detail.[66] Briefly, peptides were synthesized by solid phase Fmoc chemistry using rink-amide resin and elongated using hexafluorophosphate azabenzotriazole tetramethyl uronium (HATU) as the coupling reagent and N,N-diisopropylethylamine (DIEA) as the base. To form the staple, two naturally-occurring amino acids at discrete *i, i+4* positions were replaced with non-natural S-pentenyl alanine pairs followed by olefin metathesis using the Grubb's first-generation catalyst. Peptides were deprotected and cleaved from the resin by a solution of 95:2.5:2.5 (v/v) TFA/TIS/H_2O and purified to >95% homogeneity by C18 reverse phase HPLC (Agilent 1260 Infinity II) using an MeCN/H_2O gradient containing 0.1% TFA. Peptides were lyophilized and stored at −20°C until use.

Fluorescence Polarization Binding Assays

FP assays were performed as described previously.[67] Briefly, BAX_M, BAX_O, BCL-w_M, and BCL-w_D were serially diluted 2-fold from starting concentrations of 1.25 μM (BCL-w) or 10 μM (BAX) into assay buffer (0.01% Triton X-100 in 20 mM HEPES, pH 7.2, 150 mM KCl) in 96-well plates. FITC-peptide (3 nM) was then added and the mixture incubated in the dark for 30 min at 25°C. Fluorescence (485 nm excitation, 525 nm emission) was detected on a SpectraMax M5 microplate reader (Molecular Devices) and data subjected to nonlinear regression analysis using Prism software (GraphPad) to calculate EC_{50}s.

Hydrogen Deuterium Exchange Mass Spectrometry

BAX_O, BCL-w_D, and BCL-w_M (30 μM) were incubated individually or as BAX_O:BCL-w_D (1:4) or BCL-w_D:BAX_O (1:4) mixtures for 15 min at 23 °C in buffer (20 mM HEPES-KOH, 150 mM KCl, 5 mM $MgCl_2$, pH 7.2) prior to deuterium labeling. For stapled α1 peptide studies, BAX_O or BCL-w_D were incubated (30 μM) with vehicle, or SAH-BCL-$w_{\alpha1}$ or SAH-$BAX_{\alpha1}$ (protein:peptide, 1:5), respectively, for 1 h at 23 °C in buffer (as above) prior to deuterium labeling. Deuterium labeling of the mixture (2 μL sample) was then initiated with an 18-fold dilution into D_2O labeling buffer (36 μL, 20 mM HEPES-KOH, 150 mM KCl, 5 mM $MgCl_2$, pD 7.6, 99.9% D_2O). The labeling reaction was quenched over time (10 sec, 30 sec, 1 min, 10 min) by the addition of 38 μL of ice-cold quenching buffer (200 mM sodium phosphate, 4 M guanidinium chloride, 0.72 M TCEP pH 2.3, H_2O) and analyzed immediately. Deuterated and control samples were digested online at 15 °C using an AffiPro Nep-2 column (AffiPro, AP-PC-004). The cooling chamber of the HDX system, which housed all of the chromatographic elements, was held at 0.0 ± 0.1 °C for the duration of measurements. Peptides were trapped and desalted on a VanGuard Pre-Column trap (2.1 mm × 5 mm, ACQUITY UPLC BEH C18, 1.7 μM [Waters, 186002346]) for 3 min at 100 μL/min. Peptides were eluted from the trap using a 5%-35% gradient of acetonitrile with 0.1% formic acid over 6 min at a flow rate of 100 μL/min, and separated using an ACQUITY UPLC HSS T3, 1.8 μm, 1.0 mm × 50 mm column (Waters, 186003535). The back pressure averaged ∼12,950 psi at 0 °C in 5% acetonitrile, 95% water, 0.1% formic acid buffer. To eliminate peptide carryover, a wash solution (1.5 M guanidinium chloride, 0.8% formic acid, and 4% acetonitrile) was injected over the protease column during each analytical run. Mass spectra were acquired using a Waters Synapt G2-Si $HDMS^E$ mass spectrometer in ion mobility mode. The mass spectrometer was calibrated with direct infusion of a glu-fibrinopeptide (Sigma, F3261) solution at 200 femtomole/μL at a flow rate of 5 μL/min prior to data collection. A conventional electrospray source was used and the instrument was scanned over the range 50 to 2000 m/z. The instrument was configured in accordance with the following parameters: capillary 3.2 kV, trap collision energy 4 V, sampling cone 40 V, source temperature 80 °C and desolvation temperature 175 °C. The error of determining the average deuterium incorporation for each peptide was at or below ± 0.25 Da based on deuterated peptide standards. Peptides were identified from replicate $HDMS^E$ analyses of undeuterated control samples using PLGS 3.0.1 (Waters Corporation). Peptide masses were identified from searches using non-specific cleavage of a custom database containing the sequence of BAX (UniProt: Q07812) or BCL-w (UniProt: Q92843), no missed cleavages, no post-translational modifications, low energy threshold of 135, elevated energy threshold of 35, and an intensity threshold of 500. No false discovery rate (FDR) control was performed. The peptides identified in PLGS (excluding all neutral loss and in-source fragmentation identifications) were then filtered in DynamX 3.0 (Waters Corporation), implementing a minimum products per amino acid cut-off of 0.3 and at least 3 consecutive product ions. Peptides that met the filtering criteria were further processed by DynamX 3.0 (Waters Corporation). The relative amount of deuterium in each peptide was determined by the software, which subtracted the centroid mass of the undeuterated form of each peptide from the deuterated form at each time point and for each condition. Deuterium levels were not corrected for back exchange and thus reported as relative.[68]

Preparation of Liposomes

Large unilamellar vesicles (LUVs) were generated as previously described.[24,69] Briefly, lipid films were generated by mixing phosphatidylcholine, phosphatidylethanolamine, phosphatidylinositol, dioleoyl phosphatidylserine, and tetraoleolyl cardiolipin (Avanti Polar

Lipids) in chloroform at a molar ratio of 48:28:10:10:4, respectively, and 1 mg aliquots dried under nitrogen gas and then by high vacuum overnight. The lipid films were stored at -80 °C under a nitrogen atmosphere until use. To produce LUVs, the lipid film was resuspended in Liposomal Release Assay Buffer (10 mM HEPES pH 7, 200 mM KCl, 1 mM $MgCl_2$) containing 12.5 mM ANTS and 45 mM DPX. Liposomes were formed by 10 freeze/thaw cycles and extrusion (11 times) through a 100 nM polycarbonate membrane, and then further purified by Sepharose CL-2B size exclusion chromatography (GE Healthcare).

Chemical Crosslinking and Mass Spectrometry Analysis

Chemical crosslinking reactions were carried out as previously described.[14,22] Briefly, the BS2G crosslinker (ThermoFisher Scientific) was added at a final concentration of 1.5 mM in 0.1 M HEPES, pH 7.8, 150 mM NaCl. Zero-length EDC crosslinking reactions were performed at a final concentration of 50 mM EDC, while the Extended-EDC reactions contained 75 mM EDC and 25 mM 2,2′-(ethylenedioxy)bis(ethylamine) EDDA (Sigma). All EDC-based reactions also contained 20 mM sulfo-NHS in 0.1M MOPS buffer, pH 7.0, 100 mM NaCl. Reactions with single species (BAX_O, BCL-w_M, or BCL-w_D) were performed in a final volume of 70 μL (10 μg protein, 7 μM), whereas the reactions with the protein mixture (equimolar BAX_O and BCL-w_D based on monomeric content) were conducted in 140 μL (10 μg/3.5 μM of each protein) after a 15-min preincubation. The reactions were allowed to proceed for 60 min at room temperature with gentle agitation and then quenched with hydroxylamine to a final concentration of 100 mM for 20 min. Crosslinked samples were subjected to SDS-PAGE electrophoresis and visualized by Pierce Silver Stain kit in accordance with the manufacturer's instructions (ThermoFisher) and by western blot analysis using BAX (Santa Cruz Biotechnology Cat# sc-20067; RRID: AB_626726) and BCL-w (Cell Signaling Technology Cat# 2724S; RRID: AB _10691557) antibodies. All samples were lyophilized, resuspended in 8M urea, 50 mM EPPS, pH 8.5, reduced with addition of 10 mM TCEP for 30 min, alkylated with 30 mM iodoacetamide in the dark for 30 min, and then quenched with 50 mM β-mercaptoethanol. The samples were diluted with 50 mM EPPS to reduce urea concentration down to 1 M and then digested with trypsin (Promega) at 1:25 enzyme:substrate ratio overnight at 37°C. The digested peptides were acidified with 10% formic acid to pH ~2, desalted using stage tips with Empore C18 SPE Extraction Disks (3M), and then dried under vacuum.

Each sample was reconstituted in 5% formic acid (FA)/5% acetonitrile and analyzed in the Orbitrap Xploris 480 Mass Spectrometer (ThermoFisher Scientific) coupled to an EASY-nLC 1200 (ThermoFisher Scientific) ultra-high pressure liquid chromatography (UHPLC) pump. Peptides were separated on an in-house packed 100 μm inner diameter column containing 30 cm of Accucore C18 resin (2.6 μm, 150 Å, ThermoFisher), using a gradient of 5%–35% (ACN, 0.125% FA) over 75 min at ~500 nL/min. The instrument was operated in data-dependent mode. FTMS1 spectra were collected at a resolution of 120K, with maximum injection time of 50 ms. The most intense ions were selected for MS/MS for 1.5 s in top-speed mode. Precursors were filtered according to charge state (allowed $3 \leq z \leq 7$) and monoisotopic peak assignment was turned on. Previously interrogated precursors were excluded using a dynamic exclusion window (60 s ± 10 ppm). MS2 precursors were isolated with a quadrupole mass filter set to a width of 0.7 m/z. Precursors were analyzed by FTMS2, with the Orbitrap operating at 30K resolution and maximum injection time of 150 ms. Precursors were then fragmented by high-energy collision dissociation (HCD) at a 28% normalized collision energy.

Mass spectra were processed using a sequence database containing contaminating *E. coli* proteins, common contaminants, and BAX and BCL-w proteins. Concatenated reversed sequences were searched for Target/Decoy-based FDR estimation.[70] Precursor tolerance was set to 15 ppm and fragment ion tolerance to 10 ppm. Methionine oxidation and N-terminal protein acetylation were set as variable modifications in addition to mono-linked masses of +130.110613 for the Extended-EDC diamine crosslinker and +114.03169 for BS2G. Crosslinked peptides were searched assuming zero-length (−18.010565), Extended-EDC (+112.100048) or BS2G (+96.02113) modification masses, respectively. Crosslinked searches included 50 protein sequences to ensure sufficient statistics for FDR estimation and required at least 4 amino acids in the shortest peptide. Matches were filtered to 1% FDR on the unique peptide level using linear discriminant features as previously described.[22] Label-free quantitation of crosslinked peptides was performed In Skyline v20,[71] filtering out peaks with IdotP < 0.75.

Membrane Curvature Analyses by Small Angle X-ray Scattering

Lyophilized phospholipids 1,2-dioleoyl-sn-glycero-3-phosphoethanolamine (DOPE), 1,2-dioleoyl-sn-glycero-3-phosphocholine (DOPC), and cardiolipin (CL) (Avanti Polar Lipids) were dissolved in chloroform at 20 mg/mL to produce individual stock solutions. Three-component and pure single-component lipid compositions were prepared from these stock solutions as mixtures of PE/PC/CL at a molar ratio of 75/20/5 and 100% PE. The resulting mixture was then evaporated under nitrogen and left to desiccate overnight under a vacuum to form dry lipid films. Lipid films were resuspended in physiologic aqueous buffer (150 mM NaCl, 20 mM HEPES, pH 7.4) to a concentration of 20 mg/mL. The lipid suspensions were incubated at 37°C and then sonicated until they appeared clear. The resulting solution was extruded through a 0.2 μm pore Anotop syringe filter (Whatman) to produce small unilamellar vesicles (SUVs). BAX_O and BCL-w species were mixed with SUVs at the indicated concentrations. Precipitated protein–lipid complexes were transferred into 1.5 mm quartz capillaries (Hilgenberg GmbH, Mark-tubes) and hermetically sealed with an oxygen torch. SAXS measurements were taken at the Stanford Synchrotron Radiation Lightsource (SSRL) (beamline 4-2) using monochromatic X-rays with energies of 9 keV and 1.7m flightpath. Samples were centrifuged before measurement. The 2D powder diffraction patterns were azimuthally integrated into 1D patterns using the Nika1 1.76 package for Igor Pro 9 (Wavemetrics). To analyze the SAXS data, the integrated scattering intensity $I(q)$ was plotted against q using MATLAB. The different phases present in each sample were determined by comparing the ratios of the measured peak positions ($q_{measured}$) with those of the permitted reflections for various

liquid-crystalline lipid phases. Multiple measurements were taken for each sample to ensure consistency. The cubic phases that were observed in our experiments belonged to two different space groups, *Pn3m* and *Im3m*. The *Pn3m* space group permits reflections at ratios of $\sqrt{2}:\sqrt{3}:\sqrt{4}:\sqrt{6}:\sqrt{8}:\sqrt{9}$, while the *Im3m* space group permits reflections at ratios of $\sqrt{2}:\sqrt{4}:\sqrt{6}:\sqrt{8}:\sqrt{10}:\sqrt{12}:\sqrt{14}:\sqrt{16}$. For each cubic phase, the measured peak positions were related to the Miller indices (h,k,l) of their observed reflections with the equation $q = 2\pi\sqrt{h^2+k^2+l^2}/a$, where a is the lattice parameter of the cubic phase. The slope of the linear regression for measured q-values versus $\sqrt{h^2+k^2+l^2}$ was then used to calculate the lattice parameter. Hexagonal phases exhibit ratios of $\sqrt{1}:\sqrt{3}:\sqrt{4}:\sqrt{7}:\sqrt{9}:\sqrt{12}:\sqrt{13}$ and the slope of regression is $q = 4\pi\sqrt{h^2+hk^2+k^2}/a_{hexagonal}\sqrt{3}$, where $a_{hexagonal}$ is the lattice constant of the hexagonal phase.

Mitochondrial Cytochrome *c* Release Assays

Mitochondria from the livers of AlbCre^{pos}*Bax*$^{f/f}$*Bak*$^{-/-}$ mice were isolated as previously described.[24] Recombinant BAX_O (100 nM), or BAX_M (100 nM) with or without tBID (20 nM) and ABT-737 (100-500 nM), was incubated with or without wild-type or mutant BCL-w_M (100 nM), BCL-w_D (25-100 nM), BCL-X_{LM} (100 nM), or BCL-X_{LD} (25-100 nM) protein for 30 min, and then the protein samples added to mitochondria (1 mg/mL) in experimental buffer (200 mM mannitol, 68 mM sucrose, 10 mM HEPES-KOH [pH 7.4], 110 mM KCl, 1 mM EDTA, protease inhibitor) for 45 min at room temperature. The pellet and supernatant fractions were isolated by centrifugation and cytochrome *c* was quantitated using a colorimetric ELISA assay (R&D Systems), per the manufacturer's protocol. Percent cytochrome *c* released into the supernatant (% cytochrome *c* release) was calculated according to the following equation: % cytochrome *c* release = [cytochrome c_{sup}]/[cytochrome c_{max}]*100, where cytochrome c_{sup} and cytochrome c_{max} represent the amount of cytochrome *c* detected in the supernatant upon treatment of mitochondria with the indicated conditions or 1% (v/v) Triton X-100, respectively.

Mitochondrial Translocation and Retrotranslocation Assays

Mitochondria from the livers of AlbCre^{pos}*Bax*$^{f/f}$*Bak*$^{-/-}$ mice were isolated as described.[24] Mitochondria (20 mg/mL) were preincubated with either BAX_O or BCL-w_D at the indicated concentration (calculated by monomer) for 15 min at room temperature. Samples were then centrifuged at 5500 x *g* for 15 min at 4°C to isolate the mitochondrial pellet, which was gently resuspended in experimental buffer (200 mM mannitol, 68 mM sucrose, 10 mM HEPES-KOH [pH 7.4], 110 mM KCl, 1 mM EDTA, protease inhibitor). Either BAX_O, wild-type or E4A-mutant BCL-w_M, wild-type or E4A-mutant BCL-w_D, BCL-X_{LM}, or BCL-X_{LD} was added at the indicated ratios to the resuspended mitochondria for 30 min at room temperature. The supernatant and pellet were separated by centrifugation at 8000 x *g* for 15 min at 4°C. The pellets were resuspended with experimental buffer containing 1% Triton X-100. The supernatant and mitochondrial pellet samples were analyzed by gel electrophoresis and western blot analysis using BAX (Santa Cruz Biotechnology Cat# sc-20067; RRID: AB_626726), BCL-w (Cell Signaling Technology Cat# 2724S; RRID: AB _10691557), BCL-X_L (Santa Cruz Biotechnology Cat# sc-8392; RRID: AB_626739), and VDAC1 (Santa Cruz Biotechnology Cat# sc-390996; RRID: AB_2750920) antibodies.

Cellular Analysis of Reconstituted MEFs

Human BCL-w constructs (wild-type, G94E, E4A, G94E/E4A) were cloned (Azenta Life Sciences) into the pMIG II (pMSCV-IRES-GFP II) vector (Addgene #52107) and confirmed by DNA sequencing. Transfection of the packaging cell line GPG-293 yielded amphotropic retroviral particles, which were collected by filtration and ultracentrifugation, and then used to reconstitute *Bcl-w*$^{-/-}$ MEFs with wild-type BCL-w and the indicated mutants, as described.[55] The reconstituted MEFs were sorted for GFP-positivity over two to three rounds of flow cytometry to ensure comparable levels of expression. Transduction was verified by BCL-w western analysis using the 31H4 antibody (Cell Signaling Technology Cat# 2724S; RRID: AB _10691557, 1:1000). Cells were maintained in Dulbecco's Modified Eagle Medium (GIBCO) with 10% FBS, 100 U/mL penicillin and streptomycin, and 2 mM glutamine. Cells were verified as mycoplasma-negative using the MycoAlert mycoplasma detection kit (Lonza Biologics). For fractionation studies, cells ($1.2x10^7$) were incubated in ice-cold lysis buffer (LB) (10 mM Tris [pH 7.5], 1 mM EGTA, 200 mM sucrose, protease inhibitor) for 10 min, followed by Dounce homogenization. Lysates were centrifuged at 700 x *g* for 10 min at 4 °C to remove any unlysed cells and then supernatants centrifuged at 12,000 x *g* for 10 min at 4 °C, yielding a cytosolic supernatant fraction and heavy membrane pellet containing mitochondria. The pellet was resuspended in LB containing 2% CHAPS. Protein concentration was measured by BCA assay (ThermoFisher). The supernatant and pellet samples were analyzed by gel electrophoresis and western blotting, using BAX (B-9; Santa Cruz Biotechnology sc-7480; RRID:AB_626729), BCL-w (31H4; Cell Signaling Technology Cat# 2724S; RRID: AB_10691557), and VDAC1 (Santa Cruz Biotechnology sc-390996; RRID:AB_2750920) antibodies. For caspase-3/7 activation studies, cells (5 x 10^3/well) were seeded in 384-well format in 10% FBS/DMEM (phenol red free) in a black/clear bottom plate. The indicated concentrations of ABT-263 and S63845 (MedChemExpress) were added and cultures incubated for 6 hrs. Cell Event Caspase-3/7 Red (10 μL of 30 μM; Thermo) and Hoechst 33342 (5 μg/mL) were added to the 30 μL treatment volume 30 minutes prior to the endpoint. The plate was then read on an IXM C-LZR (Molecular Devices) with images captured using DAPI, GFP, and Texas Red filters. To ensure capture of cells with equal GFP expression, the brightest 10% GFP-positive cells were excluded from the analysis using Custom Module Editor and the fraction caspase-3/7 (+) cells were counted and plotted using Prism software (GraphPad). For viability studies, cells (5 x 10^3/well) were seeded in 384-well format in 10% FBS/DMEM. A 4-fold serial dilution of ABT263 (MedChemExpress) and a set concentration of S63845 (MedChemExpress), as indicated, were added. Cell viability was assayed

Please cite this article in press as: Newman et al., Inhibition of oligomeric BAX by an anti-apoptotic dimer, Cell (2025), https://doi.org/10.1016/j.cell.2025.10.037

at the indicated time points by addition of CellTiter-Glo chemiluminescence reagent according to the manufacturer's protocol (Promega) and luminescence measured using an Envision microplate reader (PerkinElmer). Luminescence data were analyzed and plotted using Prism software (GraphPad).

QUANTIFICATION AND STATISTICAL ANALYSIS

Data are expressed as mean ± SD unless otherwise specified. The exact numbers of biological and technical replicates for each experiment are reported in the figure legends. Data were analyzed and plotted using Prism Software 10.0 (GraphPad).

Supplemental figures

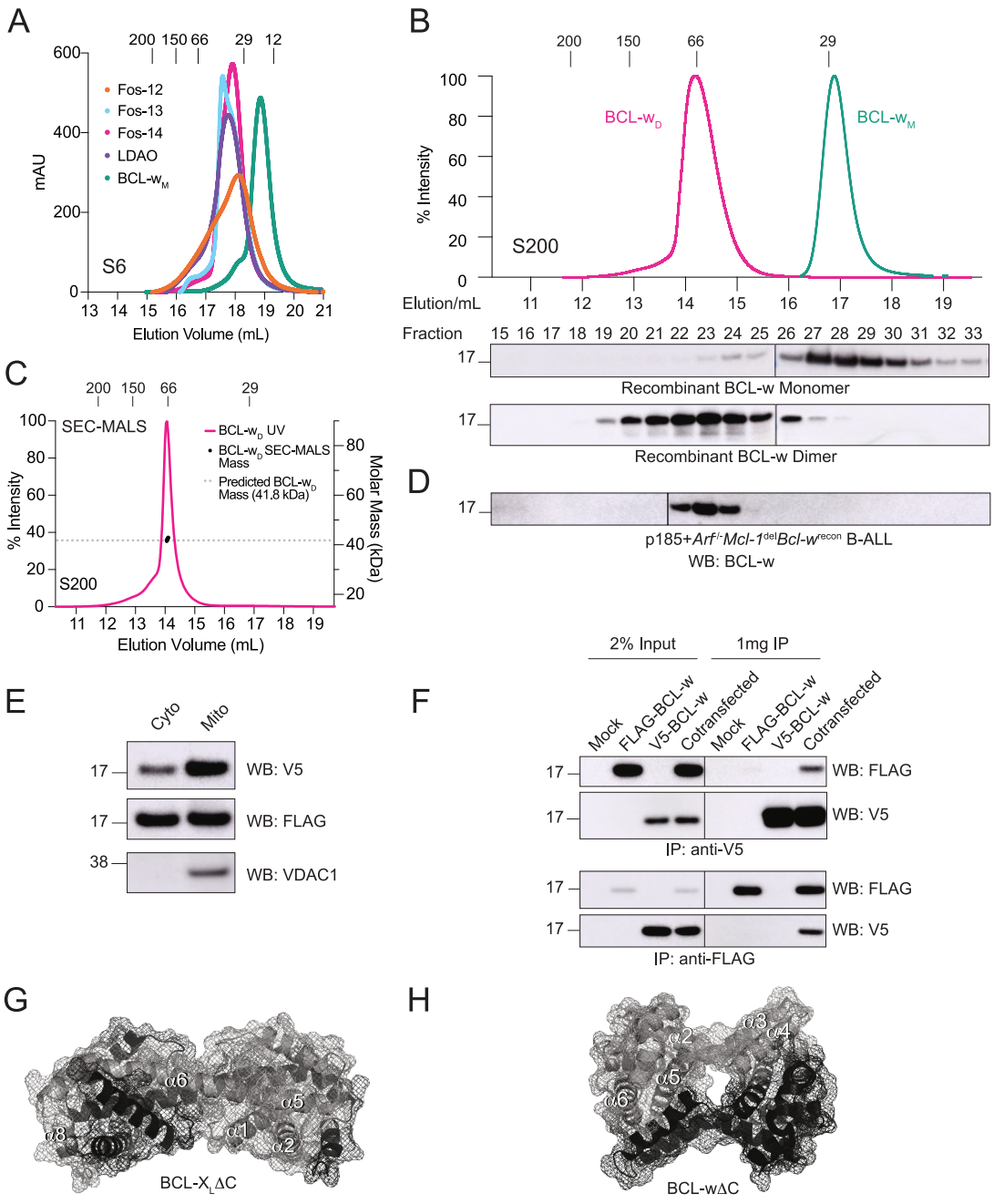

Figure S1. SEC analyses of BCL-w, assessment of BCL-w dimerization in cells, and structures of anti-apoptotic truncates, related to Figure 1

(A) SEC profiles of full-length BCL-w upon treatment with a panel of detergents using a Superose S6 column.

(B) SEC profile of BCL-w$_M$ and Fos-14-generated BCL-w$_D$ using a Superdex 200 column and BCL-w western analysis of the monomeric and dimeric fractions.

(C) SEC-MALS analysis of the BCL-w dimeric peak, confirming a molecular weight of 42 kD.

(D) Lysates from BCL-w-dependent murine leukemia cells (p185+*Arf*$^{-/-}$*Mcl-1*^{del}*Bcl-w*^{recon} B-ALL) were subjected to SEC analysis and BCL-w western blot of the indicated fractions. The detected BCL-w co-elutes in the same fractions as recombinant BCL-w$_D$.

(legend continued on next page)

(E) 293T cells were transfected with full-length FLAG- and V5-tagged BCL-w, and then cytosolic and mitochondrial fractions were isolated and subjected to FLAG, V5, and VDAC1 western analyses. Experiments were performed twice with independent preparations of cells and treatments, with similar results.
(F) 293T cells were transfected with full-length FLAG- or V5-tagged BCL-w, or both constructs, and lysates subjected to immunoprecipitation and western analysis. Experiments were performed twice with independent preparations of cells and treatments, with similar results.
(G and H) Structures of domain-swapped dimers of C-terminally truncated anti-apoptotic proteins BCL-X_L (PDB: 2B48) (G) and BCL-w (PDB: 2Y6W) (H).

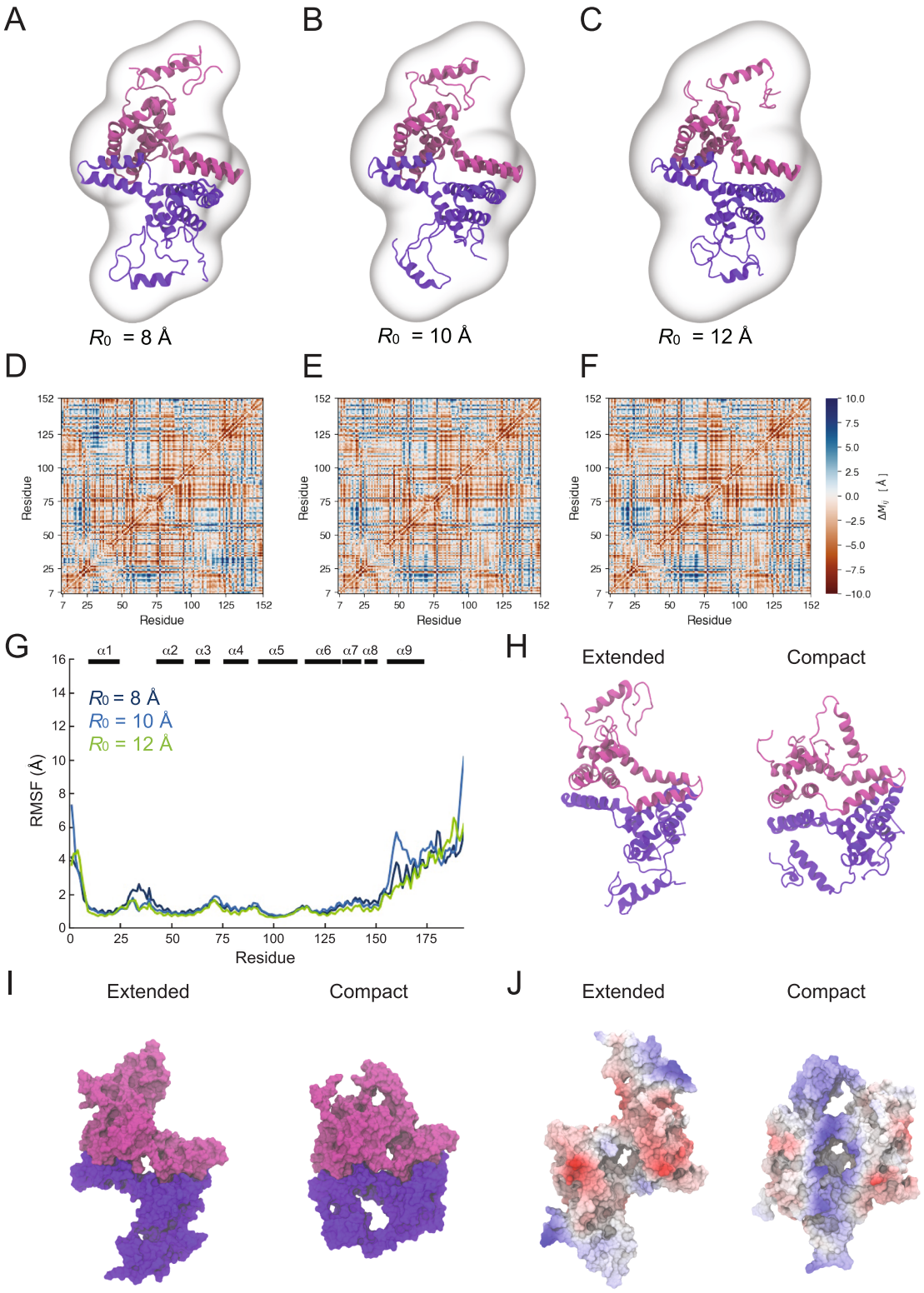

Figure S2. MD simulations and analyses of BCL-w_D structure, related to Figure 1

(A–C) Optimized model structures of BCL-w_D as calculated using a SAXS-based restraint potential at radii *R* of 8 (A), 10 (B), and 12 Å (C) (α = 1.0 kcal mol^{-1} Å^{-2}). The transparent shell is a smoothed isopotential surface at the threshold of the restraint.

(legend continued on next page)

(D–F) Difference maps $\Delta \boldsymbol{M}_{ij} = \boldsymbol{M}_{ij}^{opt} - \boldsymbol{M}_{ij}^{xrd}$ between alpha carbon (C_α) distance matrices for the shell-optimized dimers $\boldsymbol{M}_{ij}^{opt}$ with radii of 8 (D), 10 (E), and 12 Å (F), and a crystallographic counterpart $\boldsymbol{M}_{ij}^{xrd}$ (PDB: 2Y6W). The color scale highlights the differences between the MD-derived dimers and crystal structure and the consistency of these differences across the various shell-optimized dimers.
(G) Root-mean-square C_α fluctuations derived from SAXS-restrained MD trajectories in explicit solvent (5 ps sampling).
(H) Extended and compact conformers from MD trajectories without SAXS restraints. Notably, both conformers fit within the SAXS-derived envelopes.
(I) Solvent accessible surface for the extended and compact conformers of BCL-w_D, depicted with a 1.4 Å probe radius.
(J) Coloring the surface of the BCL-w_D conformers based on electrostatic potential highlights the distinctive charge distribution, which forms an electrostatic funnel in the compact species (particle mesh Ewald method; red = negative potential, blue = positive potential). The conformers shown are rotated 180° about the vertical axis relative to Figure S2I.

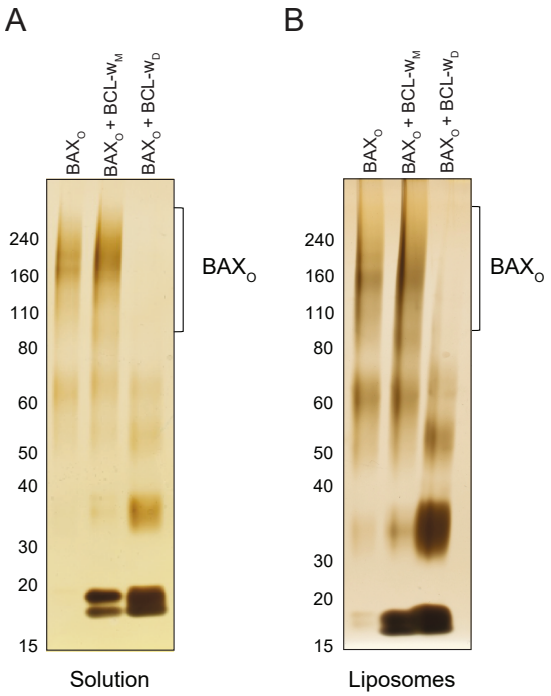

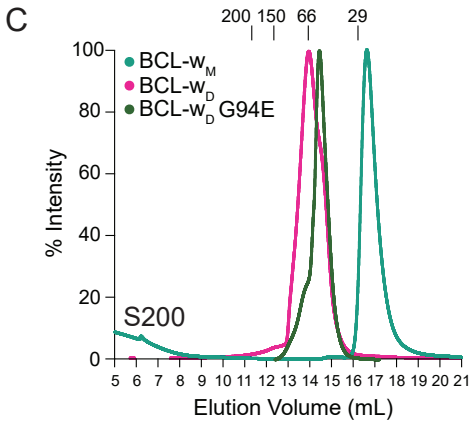

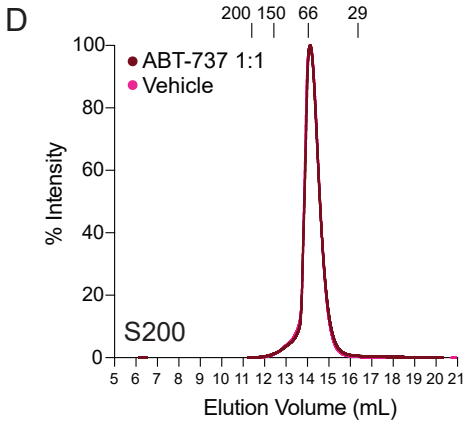

(legend on next page)

Figure S3. Chemical crosslinking analyses of BAX_O and BCL-w_M or BCL-w_D in the presence of liposomes and the effect of G94E mutagenesis and ABT-737 treatment on BCL-w dimerization, related to Figure 3

(A and B) Chemical crosslinking (EDC) of BAX_O alone or in the presence of BCL-w_M or BCL-w_D demonstrates no effect of BCL-w_M on the BAX_O laddering pattern but elimination of higher-order crosslinked bands upon treatment with BCL-w_D, as conducted in solution (A) or with liposomes that mimic the MOM lipid composition[14] (B).

(C) Fos-14 treatment of BCL-w_M G94E yields a dimer, as monitored by SEC using an S200 column.

(D) ABT-737 treatment does not disrupt dimerization of BCL-w, as monitored by SEC using an S200 column.

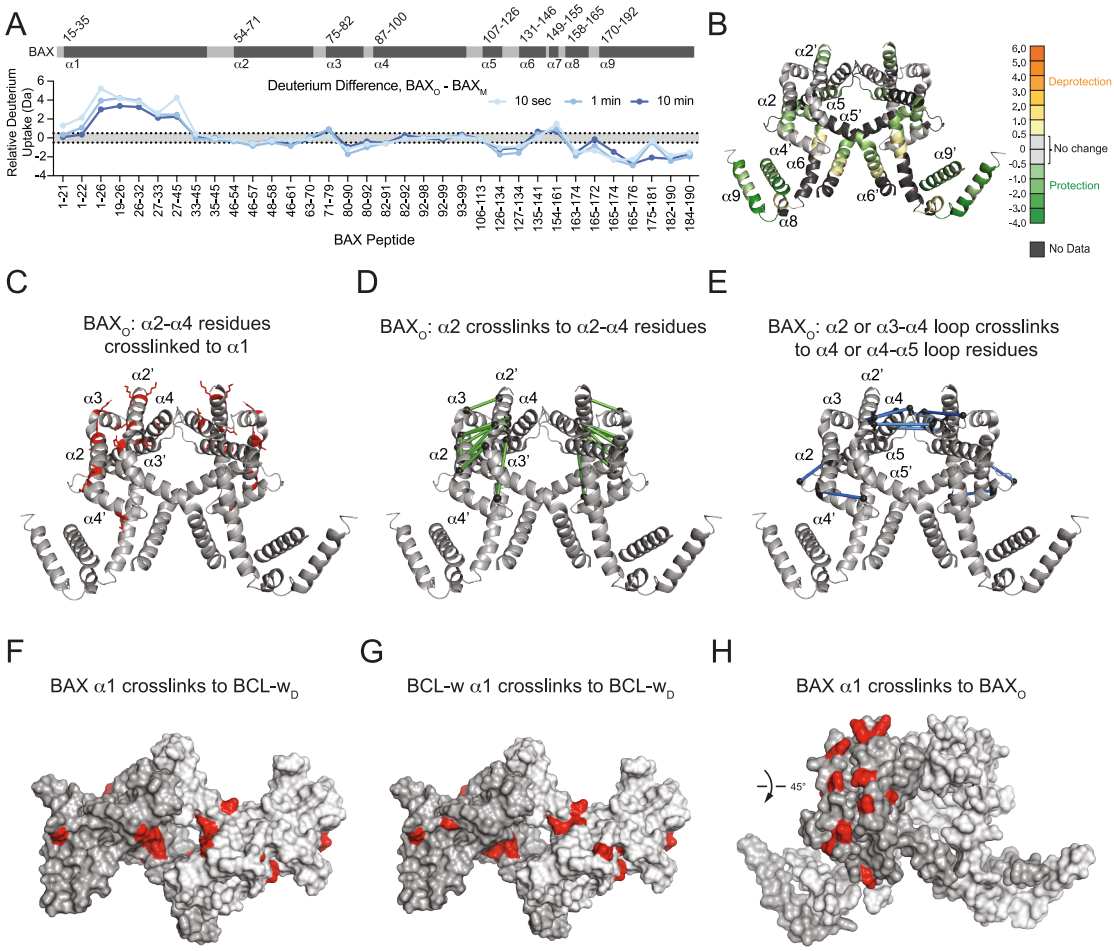

Figure S4. HDX-MS analysis of BAX$_O$ and chemical crosslinking MS analysis of BAX$_O$ upon exposure to BCL-w$_D$, related to Figure 4

(A and B) Deuterium difference plot showing the relative deuterium incorporation of BAX$_O$ minus BAX$_M$ as measured over time in solution (A), with areas of conformational deprotection and protection at 10 min (significance threshold, ±0.5 Da) mapped onto the structure of oligomeric BAX (PDB: 9IXU) (B). Prominent α1 deprotection is unmapped because that region is unresolved in the cryo-EM structure of oligomeric BAX. Data are representative of at least two independent biological replicates.

(C–E) A series of enriched crosslinks were identified in BAX$_O$ upon incubation with BCL-w$_D$, including those between BAX α1 and residues within the α1-α4 region (only α2-α4 residues are shown in red since α1 and the α1-α2 loop region are unresolved in the cryo-EM structure of oligomeric BAX) (C), between α2 and the α2-α4 region (green lines) (D), and between α2 or α3-α4 loop and α4 or the α4-α5 loop (blue lines) (E).

(F and G) Intermolecular crosslinks between BAX$_O$ and BCL-w$_D$ predominantly involve α1 residues of BAX$_O$ and α1, α2-α4, and α9 residues of BCL-w$_D$, as mapped in red for both protomers onto a surface view of the MD-derived dimeric structure (F). Intramolecular crosslinks formed between BCL-w α1 and its target residues on BCL-w$_D$ (G) are strikingly similar to those engaged by BAX$_O$ α1, as demonstrated by comparison of the surface maps (F and G).

(H) Residues involved in intramolecular crosslinks with BAX$_O$ α1 are colored red on the surface view of oligomeric BAX (PDB: 9IXU), as mapped onto one of the two asymmetric dimers for clarity. α1 is not present in the cryo-EM structure of oligomeric BAX, so crosslinked residues in this region are not mapped.

See also Tables S2 and S3 and Data S1 and S2.

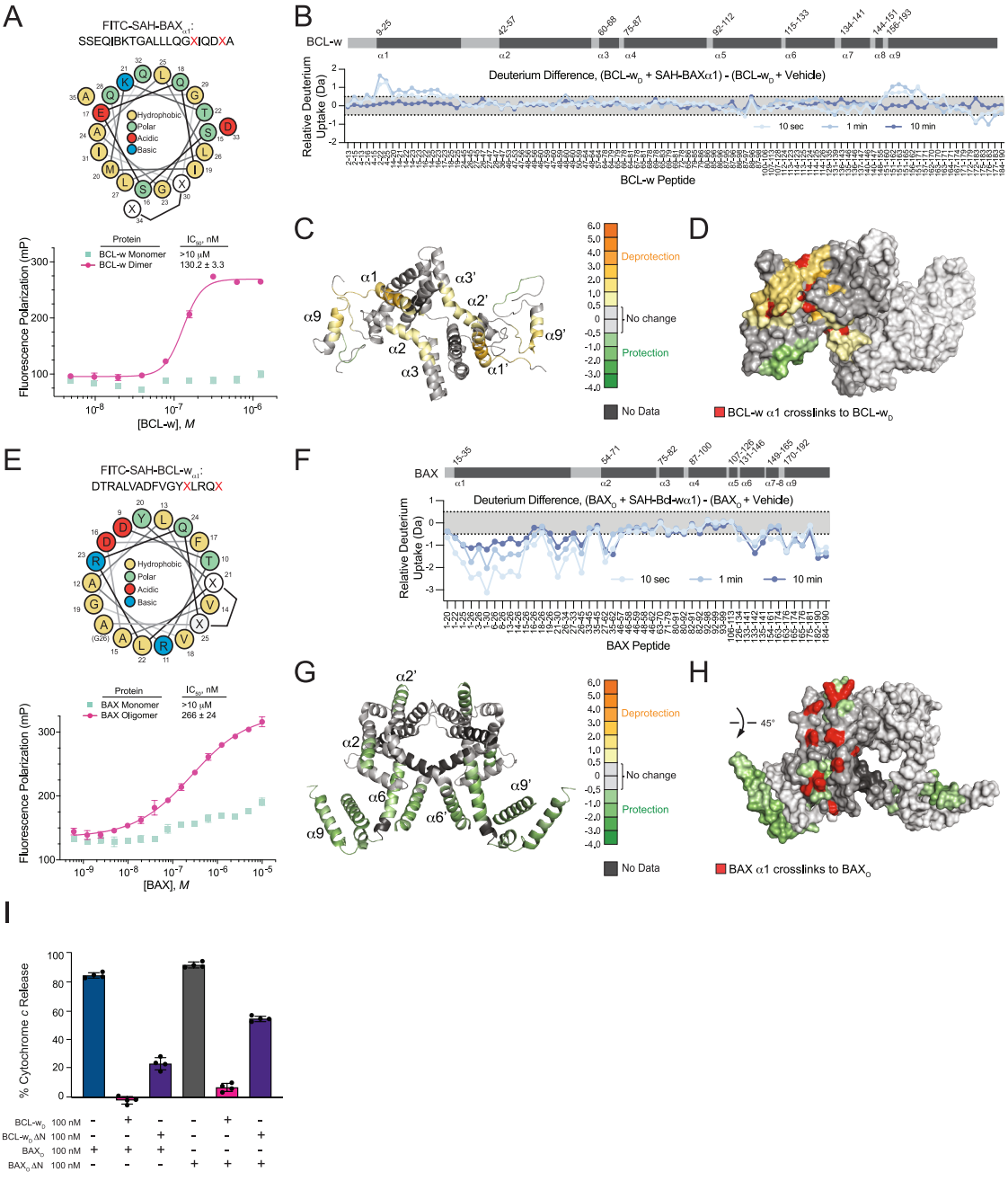

Figure S5. Reciprocal engagement of α1 helices with BAX$_O$ and BCL-w$_D$, the conformational consequences as monitored by HDX-MS, and the impact of α1 deletions on BCL-w$_D$ inhibition of BAX$_O$, related to Figure 4

(A) Helical wheel depiction of SAH-BAX$_{\alpha1}$ (X = S-pentenyl alanine, B = norleucine) and its comparative binding to BCL-w$_M$ and BCL-w$_D$, as measured by FP assay. Data are mean ± SEM for experiments performed in technical quadruplicate and repeated with independent preparations of proteins and peptides, with similar results.

(B and C) Deuterium difference plot showing the relative deuterium incorporation of BCL-w$_D$ in the presence of FITC-SAH-BAX$_{\alpha1}$ minus BCL-w$_D$ with vehicle as measured over time in solution at 10 s, 1 min, and 10 min (significance threshold, ±0.5 Da) (B) and areas of deprotection and protection at 1 min mapped onto the MD-derived structure of BCL-w$_D$ (C). Data are representative of at least two independent biological replicates.

(D) The sites of endogenous BCL-w α1 crosslinks on BCL-w$_D$ (red) co-localize with those areas of dynamic conformational change upon BCL-w$_D$ incubation with SAH-BAX$_{\alpha1}$, as mapped onto one protomer for clarity.

(E) Helical wheel depiction of SAH-BCL-w$_{\alpha1}$ (X = S-pentenyl alanine) and its comparative binding to BAX$_M$ and BAX$_O$, as measured by FP assay. Data are mean ± SEM for experiments performed in technical quadruplicate and repeated with independent preparations of proteins and peptides, with similar results.

(legend continued on next page)

(F and G) Deuterium difference plot showing the relative deuterium incorporation of BAX_O in the presence of SAH-BCL-$w_{\alpha1}$ minus BAX_O with vehicle as measured over time in solution at 10 s, 1 min, and 10 min (significance threshold, ±0.5 Da) (F) and areas of deprotection and protection at 1 min mapped onto the cryo-EM structure of oligomeric BAX (PDB: 9IXU) (G).

(H) One major area of conformational protection observed by HDX-MS upon BAX_O incubation with SAH-BCL-$w_{\alpha1}$ co-localizes with the sites of endogenous BAX α1 crosslinks on BAX_O (red), as mapped onto one asymmetric dimer unit of the tetramer for clarity. Conformational protection of the α1 region is not mapped, as that region is not present in the cryo-EM structure of oligomeric BAX (PDB: 9IXU).

(I) Effect of N-terminal deletion of BCL-w_D or BAX_O or both on the capacity of BCL-w_D to inhibit BAX_O-mediated cytochrome *c* release, as measured by ELISA assay using mitochondria isolated from AlbCre^{pos}*Bax*$^{f/f}$*Bak*$^{-/-}$ murine liver. Data are normalized to BCL-w_D constructs alone and plotted as mean ± SD for experiments performed in technical quadruplicate and repeated twice with independent preparations of proteins and mitochondria. BCL-w_D, 100 nM; BCL-w_DΔN, 100 nM; BAX_O, 100 nM; BAX_OΔN, 100 nM (concentrations calculated based on protein monomer).

See also Data S1.

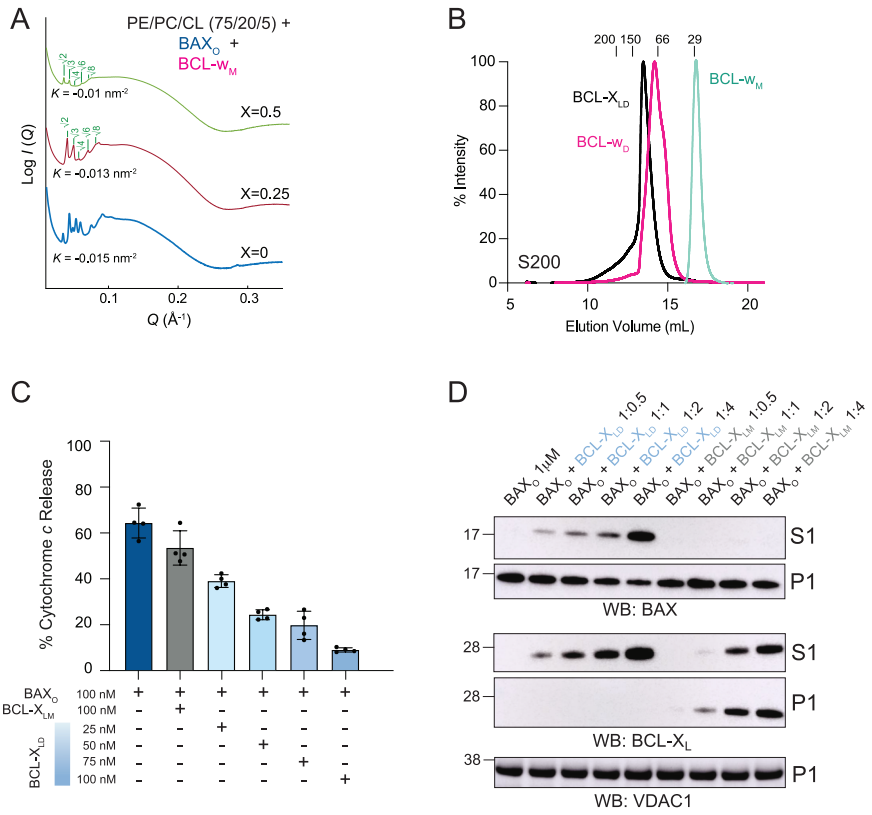

Figure S6. Dimerization of BCL-X_L, BCL-X_{LD} inhibition of BAX_O-mediated cytochrome *c* release and BAX retrotranslocation, and the effect of BCL-w_M on BAX_O NGC, related to Figure 6

(A) SAXS spectra of PE/PC/CL 75/20/5 SUVs incubated with BAX_O alone (blue trace) or in combination with increasing amounts of BCL-w_D (X = BCL-w_D:BAX_O molar ratio based on monomeric protein), demonstrating little to no blockade of BAX_O-induced NGC. Protein concentrations: BAX_O, 0.476 g/L; BCL-w_M, X = 0.25, 0.119 g/L; X = 0.5, 0.238 g/L.

(B) Fos-14 treatment of monomeric BCL-X_L yields a dimer, as monitored by SEC using an S200 column.

(C) BCL-X_{LD}, but not BCL-X_{LM}, inhibits BAX_O-mediated cytochrome *c* release from liver mitochondria isolated from AlbCre^{pos}*Bax*$^{f/f}$*Bak*$^{-/-}$ mice, as measured by ELISA assay. Data are normalized to BCL-X_L constructs alone and plotted as mean ± SD for experiments performed in technical quadruplicate and repeated twice with independent preparations of proteins and mitochondria. BAX_O, 100 nM; BCL-X_{LM}, 100 nM; BCL-X_{LD}, 25–100 nM (concentrations calculated based on protein monomer).

(D) Treatment of BAX_O-containing mitochondria with increasing doses of BCL-X_{LD}, but not BCL-X_{LM} (0.5–4 μM), leads to retrotranslocation of BAX from mitochondria to the supernatant. The experiment was performed twice using independent preparations of proteins and mitochondria, with similar results.

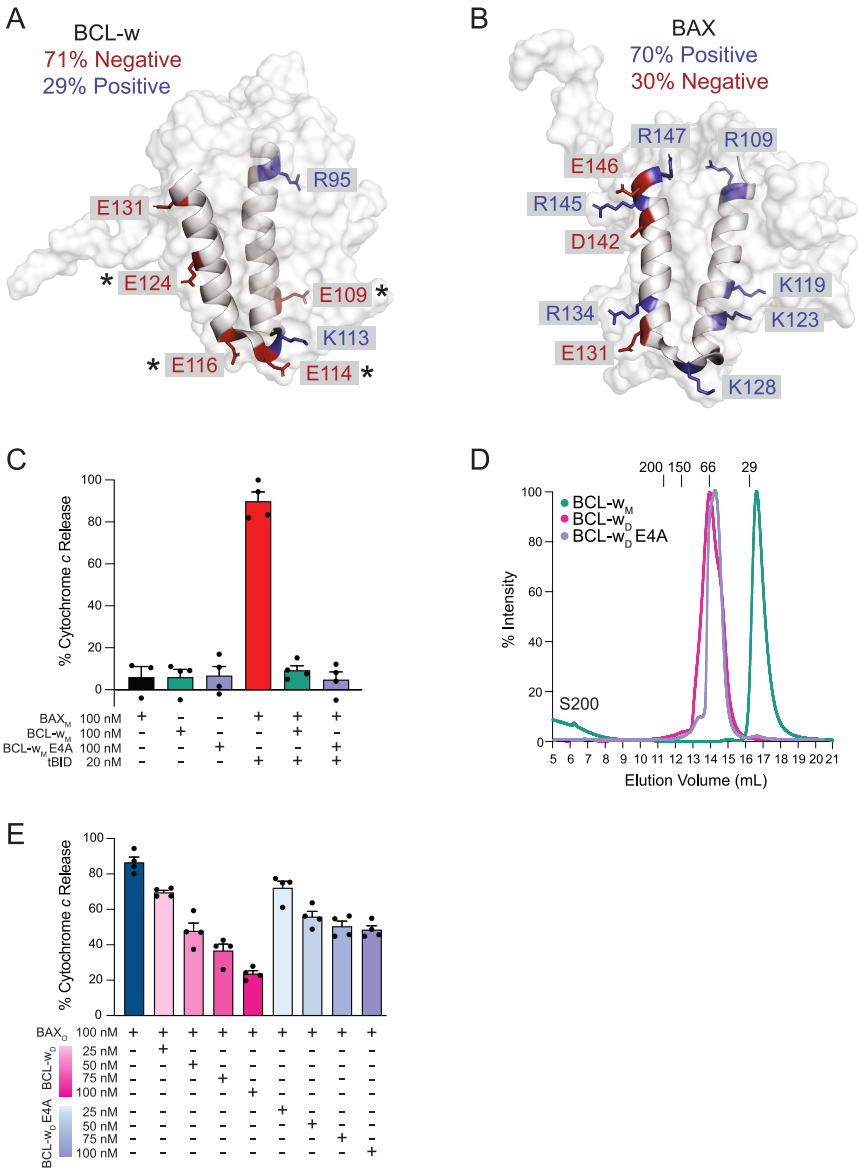

Figure S7. Design and characterization of BCL-w$_D$ E4A to dissect the non-canonical anti-apoptotic functionality of dimeric BCL-w, related to Figure 6

(A and B) Comparison of BAX (PDB: 1F16) and BCL-w (PDB: 1O0L) structures, highlighting the relative abundance of positively charged residues on the BAX α5-α6 hairpin compared with the predominance of negatively charged residues on the BCL-w α5-α6 hairpin, informing the design of BCL-w$_D$ E4A (E109A/E114A/E116A/E124A).

(C) BCL-w$_M$ E4A retains canonical groove BH3-binding activity, as demonstrated by its inhibition of tBID-triggered, BAX$_M$-mediated cytochrome *c* from liver mitochondria purified from AlbCre^{pos}*Bax*$^{f/f}$*Bak*$^{-/-}$ mice. Data are mean ± SD for experiments performed in technical quadruplicate and repeated twice with independent preparations of proteins and mitochondria. BAX$_M$, 100 nM; BCL-w$_M$, 100 nM; BCL-w$_M$ E4A, 100 nM; tBID, 20 nM.

(D) Fos-14 treatment of BCL-w$_M$ E4A yields a dimer, as monitored by SEC using an S200 column.

(E) Compared with BCL-w$_D$, BCL-w$_D$ E4A exhibits relatively impaired inhibition of BAX$_O$-mediated cytochrome *c* release. Data are normalized to BCL-w$_D$ constructs alone and plotted as mean ± SD for experiments performed in technical quadruplicate and repeated twice with independent preparations of proteins and mitochondria. BAX$_O$, 100 nM; BCL-w$_D$, 25–100 nM; BCL-w$_D$ E4A, 25–100 nM (concentrations calculated based on protein monomer).